Fall 2013

# Research on Print Defect Visibility and Evaluation

Xiaochen Jing
*Purdue University*

Graduate School ETD Form 9
(Revised 12/07)

# PURDUE UNIVERSITY
## GRADUATE SCHOOL
## Thesis/Dissertation Acceptance

This is to certify that the thesis/dissertation prepared

By Xiaochen Jing

Entitled
Research on Print Defect Visibility and Evaluation

For the degree of Doctor of Philosophy

Is approved by the final examining committee:

JAN P. ALLEBACH
Chair

MICHAEL D. ZOLTOWSKI

MIREILLE BOUTIN

ZYGMUNT PIZLO

To the best of my knowledge and as understood by the student in the *Research Integrity and Copyright Disclaimer (Graduate School Form 20)*, this thesis/dissertation adheres to the provisions of Purdue University's "Policy on Integrity in Research" and the use of copyrighted material.

Approved by Major Professor(s): JAN P. ALLEBACH

Approved by: M. R. Melloch 11-19-2013
Head of the Graduate Program Date

# RESEARCH ON PRINT DEFECT VISIBILITY AND EVALUATION

A Dissertation

Submitted to the Faculty

of

Purdue University

by

Xiaochen Jing

In Partial Fulfillment of the

Requirements for the Degree

of

Doctor of Philosophy

December 2013

Purdue University

West Lafayette, Indiana

To my parents and family.

# ACKNOWLEDGMENTS

It was a memorable and meaningful journey of pursuing my doctorate here at Purdue University. I would like to take this chance to express my thanks to the people that are significant to me and have tremendous contribution to my time here.

First of all, I deeply wish to express my sincere gratitude to my major advisor, Prof. Jan P. Allebach. His patience, encouragement, and sage advice guided me in both of my academic and personal lives. He is such a great person with compassion and wisdom. From him, I learned to think, speak, and behave logically as a professional; and be honest, humble, and amicable as a person. It was a great turning point in my life, which I got the chance to learn from him at Purdue University. I also want to thank Prof. Zygmunt Pizlo. He was the key figure in every important stages of my research process. His expertise and insightful knowledge of psychophysics have been indispensable for my entire research. I would like to send my appreciation to Prof. Mireille Boutin and Prof. Michael D. Zoltowski as well for their advice and careful guidance.

I am sincerely indebted to my parents, Wei Jing and Liya Jiang, for their unconditional and endless love, constant support, encouragement, and patience. I am grateful for their confidence and faith in me. I want to express my thanks to my husband, Kuo Guo, since he was the person who stood by me, and shared the most of delight and hard times with me here at Purdue. I also thank my son, Eric, for giving me so much pleasure and motivation. My parents and my family are the reasons that I can go this far.

I also would like to thank to my EISL colleagues, for their contribution to my psychophysical experiments. Finally, I want to thank Hewlett-Packard Company for the generous support during my Ph.D. study at Purdue.

TABLE OF CONTENTS

Page

Page

# LIST OF TABLES

# LIST OF FIGURES

# ABBREVIATIONS

| | |
|---|---|
| MMPDVP | Masking-Mediated Print Defect Visibility Predictor |
| PSNR | Peak Signal-to-Noise Ratio |
| MSE | Mean Squared Error |
| RMSE | Root Mean Square Error |
| HVS | Human Visual System |
| VDP | Visual Difference Predictor |
| VDM | Visual Discrimination Model |
| IFA | Image Fidelity Assessor |
| SSIM | Structure Similarity |
| EP | Laser Electro-Photographic |
| RIP | Raster Image Processor |
| OUM | Optimal Un-sharp Mask |
| ABF | Adaptive Bilateral Filter |
| LoG | Laplacian of Gaussian |
| MBM | Mechanical Band Measurement |
| PDVI | Predicted Defect Visibility Images |
| GTI | Ground Truth Images |
| MGTI | Modified Ground Truth Images |
| USO | Uniform Saliency-Object image |
| BTC | Block Truncation Coding |
| GMM | Gaussian Mixture Models |
| BIC | Bayesian Information Criteria |
| LUT | Look-Up Table |
| OPC | Organic Photoconductor |

| | |
|---|---|
| PQ | Print Quality |
| ROI | Region of Interest |
| JND | Just Noticeable Difference |
| ppi | pixel per inch |
| cpi | cycle per inch |
| PLUGE | Picture Line-Up Generation Equipment |
| SNR | Signal-to-Noise Ratio |

# ABSTRACT

Jing, Xiaochen Ph.D., Purdue University, December 2013. Research on Print Defect Visibility and Evaluation . Major Professor: Jan P. Allebach.

Banding is a well-known artifact produced by printing systems. It usually appears as lines perpendicular to the process direction of the print. Therefore, banding is an important print quality issue which has been analyzed and assessed by many researchers. However, little literature has focused on the study of the masking effect of content for this kind of print quality issue. Compared with other image and print quality research, our work is focused on the print quality of typical documents printed on a digital commercial printing press. In this paper, we propose a Masking Mediated Print Defect Visibility Predictor (MMPDVP) to predict the visibility of defects in the presence of customer content. The parameters of the algorithm are trained from ground-truth images that have been marked by subjects. The MMPDVP could help the press operator decide whether the print quality is acceptable for specific customer requirements. Ultimately, this model can be used to optimize the print-shop workflow.

Laser Electro-Photographic (EP) printers are complex systems that can generate prints with a number of possible artifacts that are very different in nature. It is a challenging task to develop a single processing algorithm that can effectively identify such a wide range of print quality defects. In this paper, we describe an image processing and analysis pipeline that can effectively assess the presence of a wide range of artifacts, as a general approach. In our paper, we will discuss in detail the algorithm that comprises the image processing and analysis pipeline, and will illustrate the efficacy of the pipeline with a number of examples.

Ghosting is a common print defect in Laser Electro-Photographic (EP) printing, which refers to a residual image repeat of previously printed content along the paper process direction, and appear as light or dark region relative to the surrounding field. Ghosting frequently shows in a mid-tone region following an area of solid fill. It is important to detect the location and contrast of ghosting to provide the necessary information about the ghosting source and severity. In this work, we present an algorithm for detecting and evaluating the ghosting defect. We start with a test patch design to emphasize the ghosting defect to facilitate further image processing and analysis. Moving matched filter is used to detect the ghost location along the scanned test page. The maximum Delta E as the result from the moving matched filter is used to locate and evaluate the ghosting.

# 1. MASKING MEDIATED PRINT DEFECT VISIBILITY PREDICTOR BACKGROUND

## 1.1 Introduction

### 1.1.1 Motivation

In commercial printing contexts, it is quite reasonable that customers expect good quality printed documents. Therefore, print shops need to design their work-flow to pay attention to this important aspect. This makes print quality assessment quite important for developers of commercial printing systems. However, there are not many well-developed integrated measurements of print quality. There also has been a lack of attention in the existing models to the effect of content-masking on the visibility of print defects. Furthermore, such a print quality assessment should truly represent the viewers' observations. Therefore, generating an integrated print quality model which can predict viewers' observations is difficult but greatly needed.

On one hand, the existing image quality or fidelity assessment models are mostly focused on the detection of artifacts caused by the compression of images, but not general printing defects. On the other hand, the existing print quality assessment models are most focused on assessing banding visibility with a constant gray-level background, but not natural color printouts. Furthermore, there has been a lack of attention to the content-masking effect on the print defect visibility in those models.

Compared with other image and print quality research, our work is focused on the print quality for real printouts produced by large-scale and high-end printers. We propose a masking mediated print defect visibility predictor (MMPDVP) to predict the visibility of defects in the presence of customer content. The parameters of the algorithm are trained from ground truth images that have been marked by subjects.

This predictor will help the press operator decide whether the print quality is acceptable for specific customer requirements. Hopefully, this model can be used to optimize the print-shop work-flow.

### 1.1.2 Literature review

Based on the main concerns of our research goal, we classify the research areas of our literature review into following three categories.

Typical documents printed commercially contain many images. This situation makes the images an extremely important part in print quality. Images can be produced by many devices, such as monitors, printers, and copiers, although researchers usually focus on the image quality and image fidelity which are not produced by printers but the monitors or the cameras. However, the existing image quality and image fidelity measurements are still a valuable area for us to investigate. Image quality and image fidelity are not the same, but generally they are used interchangeably [1]. Image quality refers to the preference of one image over the others, while image fidelity refers to the accuracy between two images. Here we put them into the same category, since most of the assessment models on image quality and fidelity have the same purpose.

Usually, one can describe the image quality assessment assignments in the framework of image fidelity [2]. Many basic and widely used image quality and image fidelity metrics are in this area. For image quality evaluation, there are Peak Signal-to-Noise Ratio (PSNR) and Mean Squared Error (MSE); for image fidelity evaluation, there are Root Mean Square Error (RMSE) and point-by-point $CIE\ L^*a^*b^*$. The comparison of these metrics has been done in [3, 4]. All of these metrics are convenient and computing economically, but they do not take into consideration of the perceptual process performed by Human Visual System (HVS). In the past five decades, many models have considered the performance of the HVS. Some of them are based on the pyramid structure of the HVS. These models successfully predict the response of the

visual system to a set of gray stimuli and then apply the response to a model which can predict the response of the visual system to complex images [2, 5–13]. But all these models are monochrome and cannot provide a predicted difference for natural color images. More recently, researchers have focused on how to extrapolate these existing models into a color version [14–18]. Most of these algorithms which are based on the pyramid structure of the HVS will finally provide an overall predicted map between the original image and the distorted image. Such as Daly's Visual Difference Predictor (VDP) [6], Lubin's Sarnoff Visual Discrimination Model (VDM) [2], and Christopher Taylor's Image Fidelity Assessor (IFA) [10, 11] are all approaches which provide predictions of image fidelity. Our model also accepts two kinds of images as input [19]. They are the original content image and the original content image with defect. Then this model will generate an overall predicted map showing where the viewer might observe a defect. However our model is not based on the pyramid structure of the HVS model, although it still considered the performance of HVS. There are also some algorithms that falls into this category, such as the well-known Structure Similarity (SSIM) index [20–22].

Print quality may be regarded as a special case of the more general image quality, where we specially focus on print quality issues and artifacts produced by the printing system. Therefore, one can consider print quality assessment as investigating the image quality from a different perspective. The print quality metrics evaluate perceptual difference based on the physical characteristics between the original files and the resulting prints. There has been research concentrating on investigating banding artifacts and mottle in Laser Electro-Photographic (EP) or inkjet printing systems [23–33] and toner scatter in EP systems [34, 35]. There are also some general print quality assessment models [36–39]. However most of these models are focused on assessing banding visibility with a constant gray-scale background where the banding is produced by small business or home printers.

The real printouts cannot be just constant gray-scale background. However, little research has concentrated on the content-masking effect. Researchers have noticed the

masking effect for some time [40], and most of the research has zeroed in on contrast masking [41–44]. Many studies have been done on the masking effect of the image content, but when Watson et al. first proposed the term "entropy masking" [45], researchers then started to use this terminology. Hemami et al. pointed out that masking effect is a very important element in image quality [46]. But most of the masking effect research is not focused on the natural image and print defects.

Our work has been heavily influenced by the above models and theory. The goal of our MMPDVP is to take into account the content-masking effect of content produced by a commercial high-end digital press. MMPDVP also considers the HVS's perceptual process by training the parameters on ground truth images which are marked by subjects in our psychophysical experiments. Furthermore, since banding is one of the most common print defects, we will take banding artifact as our first target print defect and provide a final prediction map that shows where the viewer will observe banding. Figure 1.1 indicates that MMPDVP accepts two images as input and produces one prediction map as output.

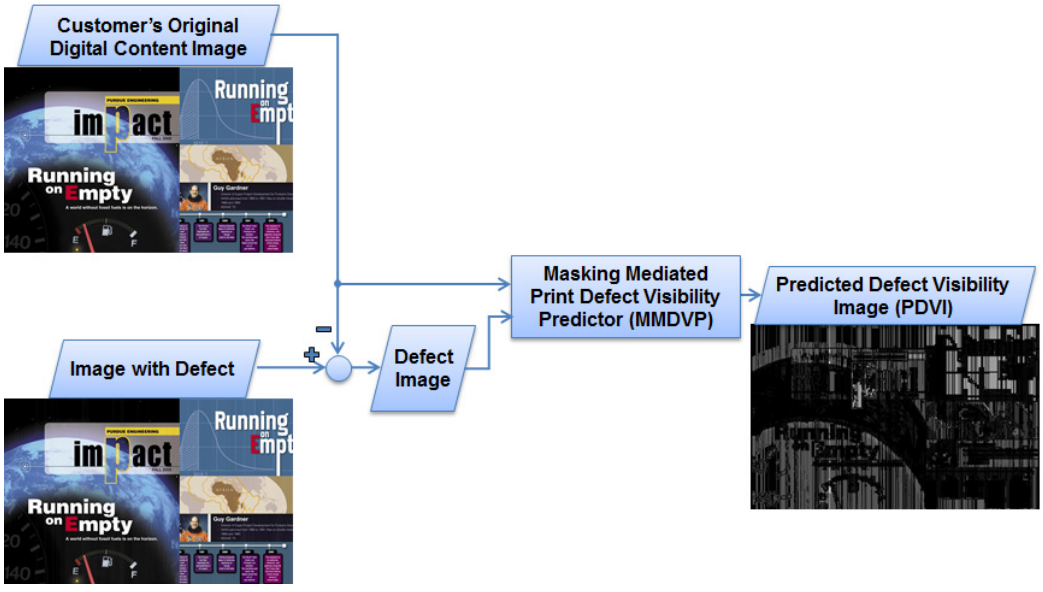


Fig. 1.1. The masking mediated print defect visibility predictor (MMPDVP) accepts two images as input and produces one prediction map the predicted defect visibility image (PDVI) as output.

### 1.1.3 Organization

This MMPDVP topic contains three chapters. In Section 1.2 we explain the background of the Indigo Press and the application scenario for the masking mediated print defect visibility predictor. In Chapter 2 we describe the basic idea of the psychophysical experiments that we have conducted to obtain the ground truth information. In Section 3.2 we explain the structure of the masking mediated print defect visibility predictor. In Section 3.3 we talk about the training and testing process of our model. Finally, we draw our conclusions and talk about the future work in Section 3.4.

## 1.2 Application Scenario for Masking Mediate Print Defect Visibility Predictor

### 1.2.1 Indigo Press

Indigo Press is a series of high-end large-scale digital printing presses manufactured by the Hewlett-Packard company in Israel. This series of presses are well used for general commercial printing. Except the usual function like direct mail, publications, photo, flexible packaging, labels, and folding cartons, which can also be done by most of the printers used for home office and small business. HP Indigo Press can also used for specialty printing, since this series of presses can print without films and plates. Furthermore, HP Indigo Press series have several embedded in-line scanners, which can let the operators to compare the scanned image to the digital reference image on the fly. This function enables the operators to observe the print defect, then change images, text, and jobs without stopping the press. Figure 1.2 shows a picture of HP Indigo WS6000p digital press application.

Fig. 1.2. HP Indigo WS6000p digital press application.

### 1.2.2 Application scenario for masking mediated print defect visibility predictor

Figure 1.3 shows the general framework of the application scenario for MMPDVP. The top half of the diagram indicates the process of capturing the Indigo Press defect. Raster image processor (RIP) will convert the PDF file of customer document into customer's original digital content image. Then the Indigo Press in-line scanners will scan the printout from Indigo Press in the same printing process. Finally, one can get the defect image by subtracting the scanned image with defect from the customer's original digital content image. The bottom half of the diagram shows our model MMPDVP. The MMPDVP accepts the customer's original digital content image and defect image as input and produces one predicted defect visibility image (PDVI) as output. The gray-scale levels of the PDVI indicate the visibility of the defect. Based on the prediction of our model, black indicates that customers will not observe any defect; white indicates that there is a high probability that customers will observe the defect. The result PDVI shown in Fig. 1.3 takes banding as the example defect. Then black indicates that there is no banding, and white indicates that there is strong banding.

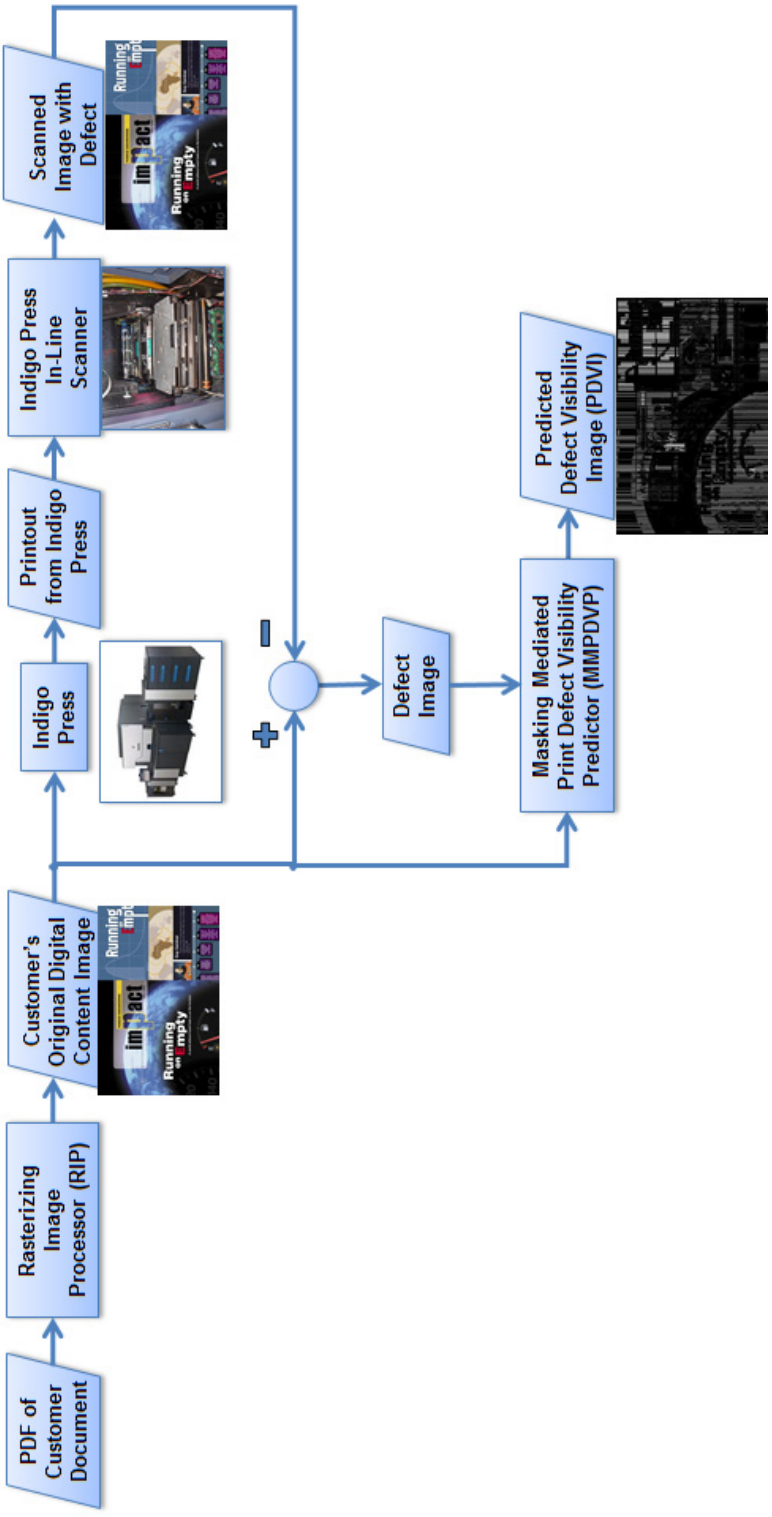


Fig. 1.3. General framework of the application scenario for MMPDVP. It accepts two images as input and produces one prediction map as output. The gray-scale levels indicate the visibility of banding. (Black indicates that there is no banding, and white indicates that there is strong banding).

# 2. MASKING MEDIATED PRINT DEFECT VISIBILITY PREDICTOR PSYCHOPHYSICAL EXPERIMENTS

## 2.1 Background

Banding is one of the most common print artifacts. It usually appears as a luminance variation and a chromatic variation across a printed page in the scan direction, which is perpendicular to the paper process direction. Figure 2.1(a) shows an example original image with the scan and print process direction. Figure 2.1(b) shows that original image with simulated banding. In the commercial contexts, the banding will not be so visible.

## 2.2 Collecting Modified Ground Truth Data as Marked by Subjects

First, to develop the MMPDVP, we simulate the kind of images that would be generated during the printing process shown in Fig. 1.3, which have banding defects on the page content. Second, in order to generate a model based on the HVS, we need to train the parameter of our model to the modified ground truth information which we can get from the psychophysical experiments. Therefore, we then use subjective experiments to assess what customers would say about defect visibility in these images.

### 2.2.1 Apparatus and conditions

For the following five psychophyical experiments, including two experiments for subject guiding rulers generation, two experiments for subject guiding rulers validation, and one experiment for collecting modified ground truth data, we all maintain the same experiment environment. We display the stimuli on an HP LCD monitor


(a) Original image.

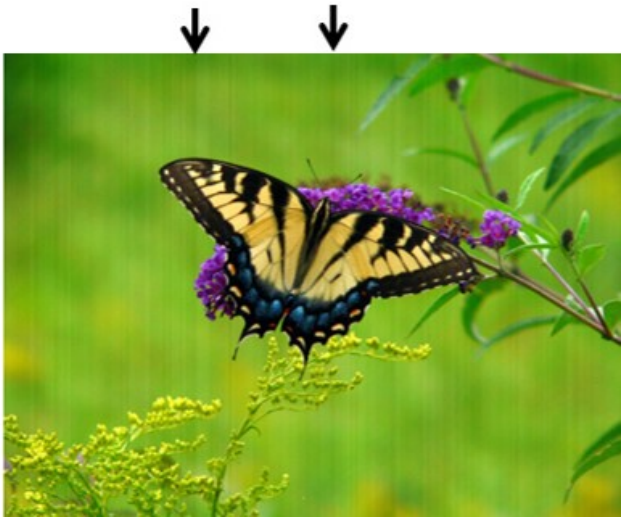

(b) Image with banding.

Fig. 2.1. Example of the original image and the image with banding.

display L2206x. The resolution of the display was set to be 100 pixel per inch (ppi) on a 1920 by 1080 pixels screen with a 60Hz refresh rate. We choose the color setting for the monitor to be 6500K. We then calibrate the monitor by using the Picture Line-Up Generation Equipment (PLUGE) test signals to adjust the brightness and contrast setting. The brightness and contrast settings are 90 (0-100) and 80 (0-100), respectively, and the gamma is 2.2. We present a mid-tone gray color as the background with two step-wedge patches on both sides of the monitor. Finally, the experiments are conducted in a dark room with all lights off and the viewing distance is 16 inches.

### 2.2.2 Subject guiding rulers generation

#### 2.2.2.1 Motivation

To collect the modified ground truth data, we conduct non-reference psychophysical experiment as described in Sec. 2.2.4. There are many ways to operate the experiment, such as pair comparison and rank order [47]. However, these methods are hard to quantify the final result. Therefore, a new method is proposed to evaluate image quality called the quality ruler method [47–50]. By simulating the defects, one can generate test pages and use those test pages as quality ruler in the subjective evaluation. There are works that focus on conducting psychophysical experiments by using the quality ruler method following the guideline of the INCITS W1.1 team and ISO 20462 [51, 52]. These reports show that the quality ruler method has its advantage for quantifying the final result. Our work of generating subject guiding rulers is largely inspired by Keelan's book and ISO image quality standards.

#### 2.2.2.2 Subject guiding rulers stimulus parameters

The subject guiding rulers use the unit of Just Noticeable Difference (JND), which provides a natural unit for quality scale calibration [47]. Since banding is perceived as one dimensional luminance and chromatic variation across a page in the scan

direction. And the luminance variation dominate the banding visibility. Therefore, we decide to use sinusoidal grating to generate our stimulus in $L^*$ channel on a mid-tone gray patch with $L^*$ channel pixel value equal to 50. The spatial frequencies of the banding that we use in the stimuli of modified ground truth experiment is from 0.5 cycle per inch (cpi) to 25 cpi. Based on that fact and the existing research of banding assessment and characterization [24, 26, 53–55], we decide the spatial frequency range of the sinusoidal grating that we add on the guiding ruler is from 5 cpi to 25 cpi. We then pick up three frequency levels from the range: 6 cpi, 12 cpi, and 24 cpi to generate the stimuli we use in the subject guiding rulers experiments. The stimulus width of 6 cpi, 12 cpi, and 24 cpi are half inch, 1 inch, and 2 inches, respectively. We define contrast as

$$C = \frac{L_{max} - L_{avg}}{L_{avg}}. \tag{2.1}$$

This definition is equavalent to the contrast definition proposed by King-Smith and Kulikowski [56] and nominal contrast defined by Watson [5]. We use percentage contrast in our experiment. To get one JND from contrast 0% for each frequency level, we then conduct the detection experiment in a similar way as reference [57, 58]. After getting one JND from contrast 0%, we use this JND patch as reference to get next level of JND by conducting discrimination experiment.

#### 2.2.2.3 Detection experiment

In a single session, the frequency of the stimulus is held constant. We use the method of constant stimuli. A fixation cross is displayed before and after each trial as shown in Fig. 2.2 of our Graphical User Interface (GUI). The stimulus is presented in the center of a uniform gray field with mid-tone gray. Within a session, we present seven levels of contrast. Each contrast level is presented 30 times. One contrast level is set at 0%, and the trials with 0% contrast served as "catch" trials. Each trial is initiated with a 50 ms average luminance uniform field with the fixation cross, then followed by a 100 ms presentation of the stimulus. The order of the trials is

randomized. The subject then press the "yes" button if he or she see the stimulus or the "no" button if he or she does not see the stimulus. Auditory feedback is provided after each catch trial presentation.

The result of each session is a psychometric function indicating the probability of detecting the sinusoidal patch at various contrast levels. Figure 2.3 shows an example of the psychometric function of frequency level 6 cpi. These data are analyzed using probit analysis to obtain the mean and standard deviation of the best fitting cumulative Gaussian distribution functions. The contrast level of the mean plus standard deviation is used as one JND [47, 59].

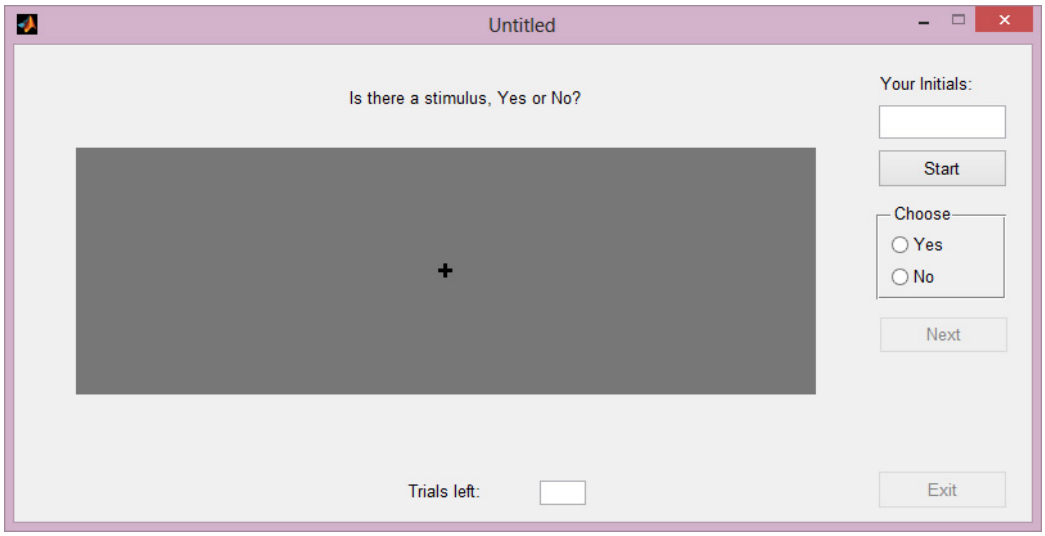


Fig. 2.2. GUI used in detection experiment.

#### 2.2.2.4 Discrimination experiment

A fixation cross remain at the center of a uniform gray image with mid-ton gray in each session. Within a session, there are six test patches, with different contrast levels. Three of them have contrast level slightly above reference contrast, while the other three have contrast level slightly below the reference contrast. In each trial, each test patch is presented 30 times. The two sinusoidal patches are presented to

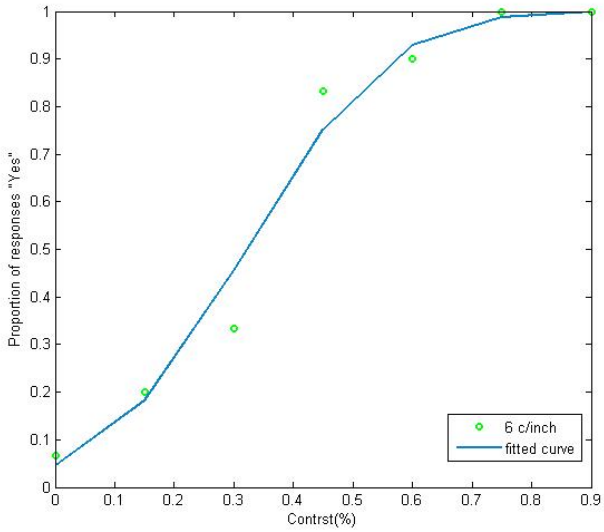


Fig. 2.3. Psychometric function for 6 cpi sinusoidal test patch on reference contrast level 0% in detection experiment.

either side of the fixation cross as shown in Fig. 2.4. The test patches are presented in random order, and the side of presentation for the test and references patches are randomized. The subject is asked to indicate which patch (left or right) had higher contrast. Auditory feedback is provided after each incorrect response. The results are analyzed using probit analysis [47, 59] to obtain JND. Figure 2.5 shows an example of the psychometric function of frequency level 24 cpi on reference contrast level 1.2%.

#### 2.2.2.5 Experimental result

We finally get ten JND levels from contrast 0% for each frequency level. Then we generate the subject guiding rulers as shown in Fig. 2.6. The three patches in each row of the ruler have the same JND level, the three patches are stimuli with sine-wave grating 24 cpi, 12cpi, 6 cpi from left to right. We put them into three categories: level 1 indicates weak banding, where the top row and bottom row have an average JND at 3; level 2 indicates medium banding, where the top row and bottom row have an

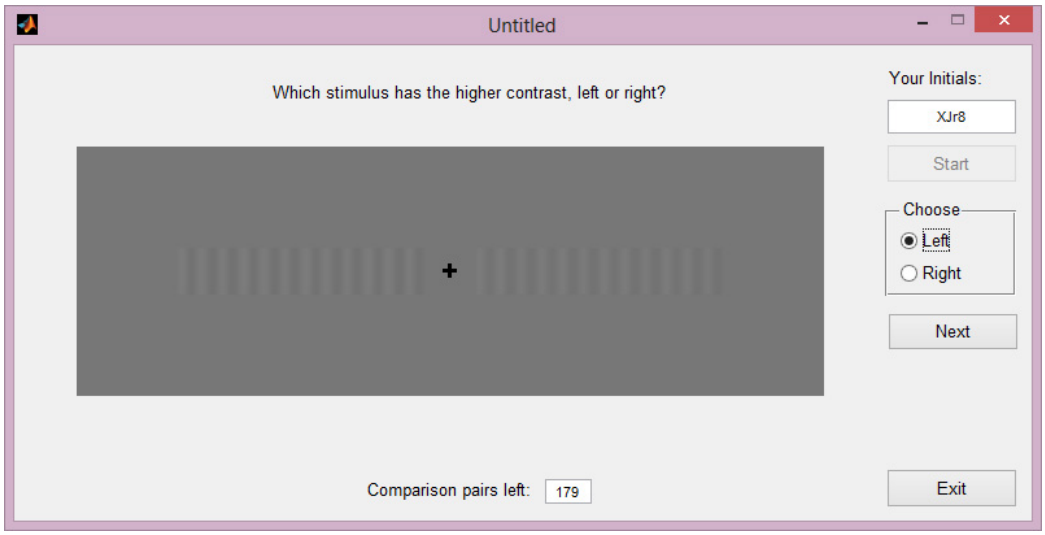


Fig. 2.4. GUI and example stimuli used in discrimination experiment.

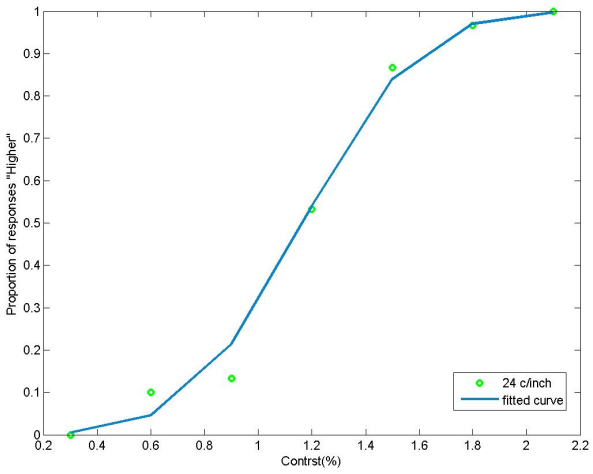


Fig. 2.5. Psychometric function for 24 cpi sinusoidal test patch on reference contrast level 1.2% in discriminate experiment.

average JND at 6; level 3 indicates strong banding, where the top row and bottom row have an average JND at 9.

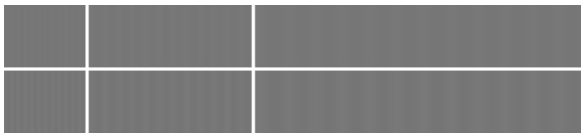

(a) Level 1 for weak banding.

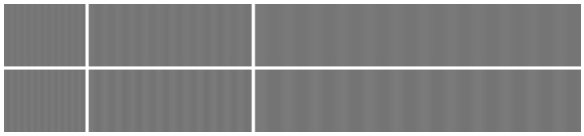

(b) Level 2 for medium banding

(c) Level 3 for strong banding.

Fig. 2.6. Subject guiding rulers.

Then in Sec. 2.2.4 for collecting the modified ground truth data, subjects are asked to mark the stimuli with natural image based on the subject guiding rulers. By having this subject guiding rulers, subjects can have an explicit definition on the banding visibility levels. Furthermore, this guiding ruler can limited the bias from stimulus to stimulus and subject to subject.

### 2.2.3 Subject guiding rulers validation

We then validate the subject guiding rulers with the following two psychophysical experiments. To conduct the two experiments, we first design six images with

Mondrian art layout, then generate sinusoidal grating within each patch of the image with different frequencies and contrast levels on mid-tone gray in the same way as we generate the rulers' patch. The positions of the sinusoidal grating among the six images are randomized. Finally, we use these six images as the stimuli in both of the two psuchophysical experiments. Figure 2.7 shows an example of the stimuli that we use. The only different between these two experiments is one experiment has rulers on the bottom of the GUI (Fig. 2.8), while the other one does not have (Fig. 2.9).

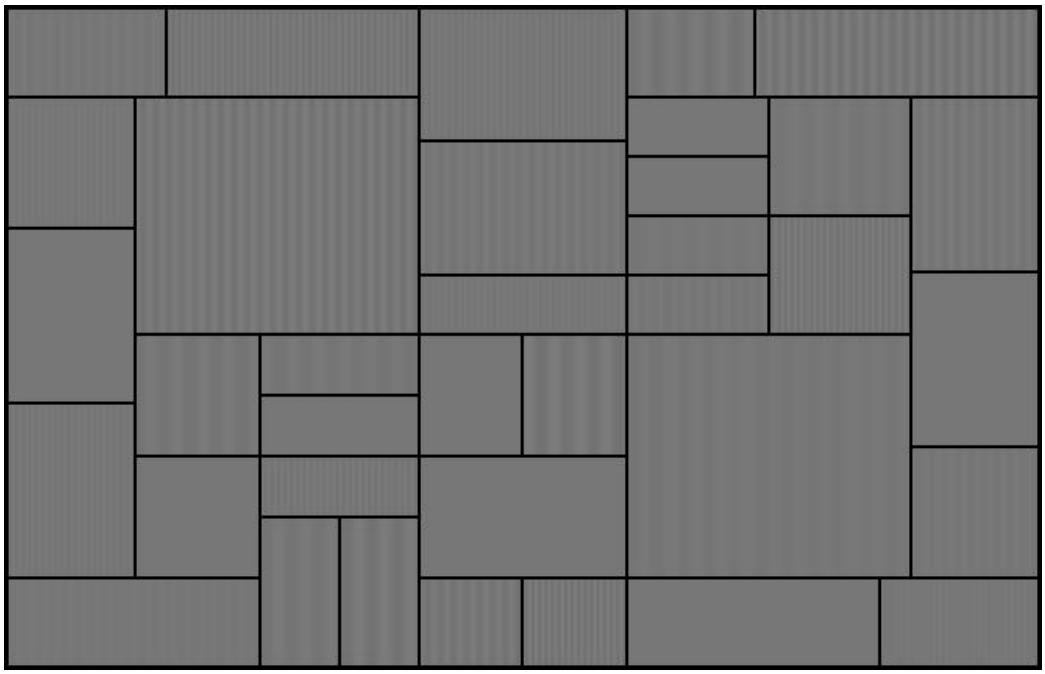

Fig. 2.7. Example of Mondrian art layout stimulus that we use in subject guiding rulers validation experiments.

The experiment setup is described as follow:

1. Twenty subjects participate in this experiment. While ten subjects participate in the experiment with rulers, ten subjects participate in the experiment without rulers.

3. One monitor with the same setup as the detection and discrimination experiment.

4. The same six stimuli are shown in both of the two experiments.

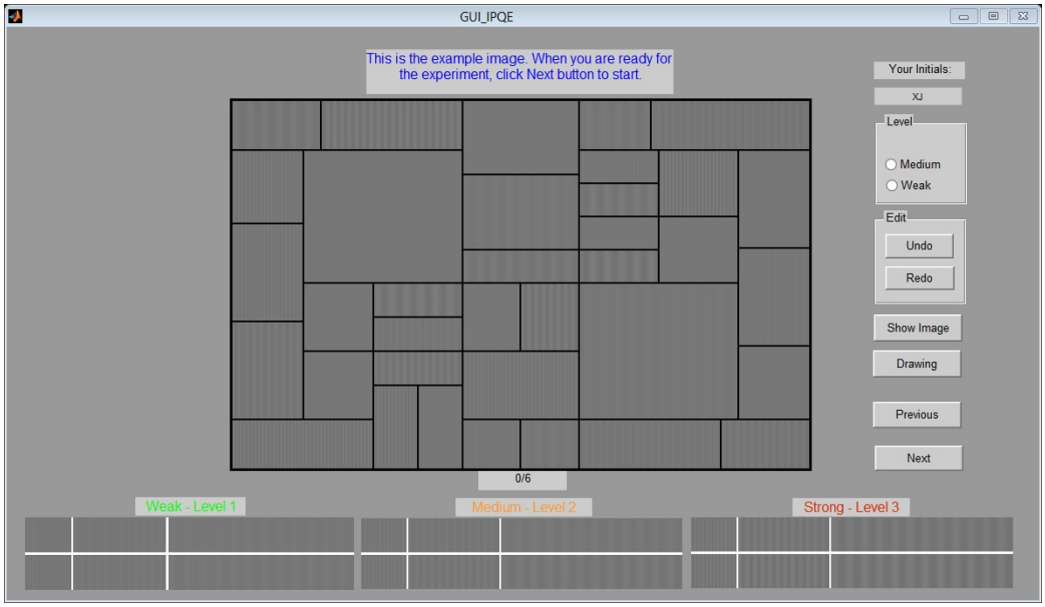


Fig. 2.8. Subject guiding rulers validation experiment with guiding rulers.

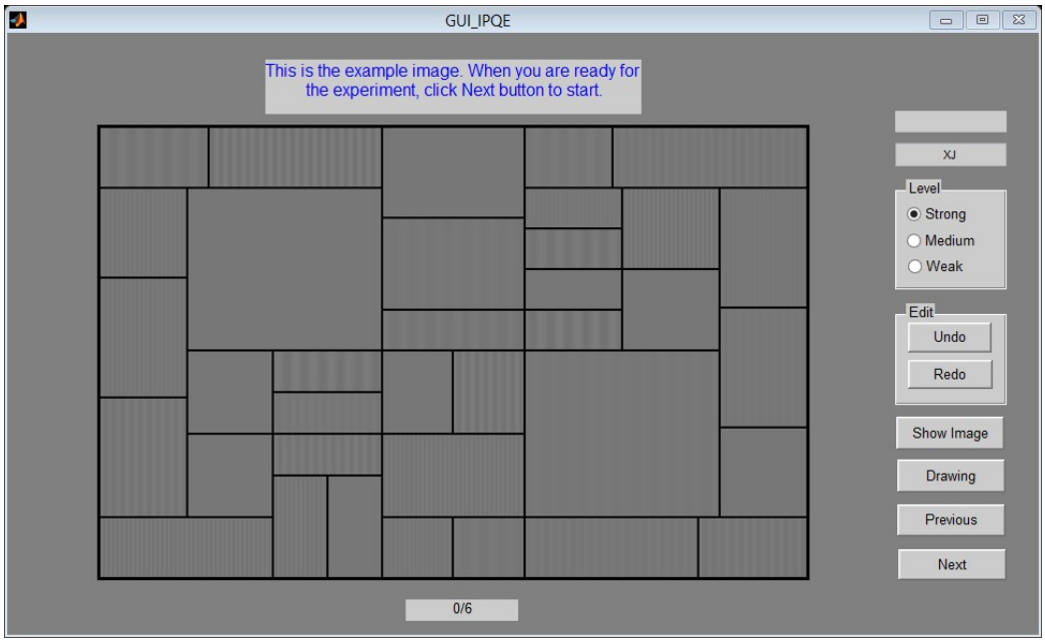


Fig. 2.9. Subject guiding rulers validation experiment without guiding rulers.

5. Step-wedge shown in Fig. 2.10 is used in a vertical direction on both sides of the GUI in our experiment to help the subject find the right view angle relative to the monitor. This simple test pattern is evenly spaced from 0 to 100 in $L^*$ channel. During the whole experiment, the subject should always try to find the right view angle so that he or she can distinguish each step.

6. Subjects can choose among three severity levels with different color of markers, where *red* means strong level, *yellow* means medium level, and *green* means weak level. Then subjects can draw rectangular mark on the stimuli within each patch to claim their opinion about the visibility of the sinusoidal grating of that patch.

7. The subjects participate in the experiment with rulers need to make their decision strictly based on the rulers, while the subjects participate in the experiment without rulers can make their own judgment.

Fig. 2.10. Example of step-wedge.

We collect the data of all the twenty subjects. Each patch of one stimuli has a record from each subject's decision. Compare the record from subjects with the correct visibility level from our rulers, we then calculate the percentage of the incorrect subject answer, and call it incorrect count (%).

Table 2.1 shows the incorrect count in percentage of the record from subjects participate in experiment with rulers. Table 2.2 shows the incorrect count in percentage of the record from subjects participate in experiment without rulers. For both of the two tables, the first column except the last two elements indicates the stimulus number, and the first row except the last two elements indicates the subject number. Furthermore, the last two columns of both tables indicate the mean and standard deviation of the data among all the subjects, while the last two rows of both tables indicate the mean and standard deviation of the data among all the stimuli. Compare

Tab. 2.1 and Tab. 2.2, we can see that the answers from subjects with rulers have a lower mean of the incorrect count among all the subjects, and the standard deviations are also lower than the answers from subjects without rulers. Furthermore, from Tab. 2.1, which shows the data from the experiment with rulers, we notice that it is critical to have responsible and skilled subjects. This is the reason we choose to use one expert subject in the following experiment.

Table 2.1
Incorrect count in percentage (%) of the record from subjects participate in experiment with rulers.

| Sti \ Sub | 1 | 2 | 3 | 4 | 5 | 6 | 7 | 8 | 9 | 10 | Mean (Sub) | Std (Sub) |
|---|---|---|---|---|---|---|---|---|---|---|---|---|
| 1 | 19.4 | 8.3 | 5.6 | 27.8 | 16.7 | 11.1 | 13.9 | 19.4 | 22.2 | 5.6 | 15 | 7.4 |
| 2 | 16.7 | 16.7 | 11.1 | 25 | 16.7 | 2.8 | 13.9 | 13.9 | 11.1 | 2.8 | 13 | 6.7 |
| 3 | 22.2 | 5.6 | 11.1 | 19.4 | 19.4 | 8.3 | 19.4 | 13.9 | 16.7 | 8.3 | 14.4 | 5.8 |
| 4 | 16.7 | 2.8 | 16.7 | 27.8 | 11.1 | 16.7 | 13.9 | 13.9 | 8.3 | 8.3 | 13.6 | 6.7 |
| 5 | 11.1 | 8.3 | 16.7 | 19.4 | 11.1 | 5.6 | 5.6 | 19.4 | 13.9 | 11.1 | 12.2 | 5.1 |
| 6 | 19.4 | 8.3 | 11.1 | 25 | 2.7 | 5.6 | 25 | 19.4 | 13.9 | 8.3 | 15.3 | 6.9 |
| Mean(Sti) | 17.6 | 8.3 | 12 | 24 | 15.3 | 8.3 | 15.3 | 16.7 | 14.4 | 7.4 | / | / |
| Std(Sti) | 3.8 | 4.6 | 4.2 | 3.8 | 3.4 | 5 | 6.5 | 3 | 4.8 | 2.9 | / | / |

### 2.2.4 Collecting modified ground truth data

After we generate the subject guiding ruler, we then start the process of collecting modified ground truth data. This process is shown in Fig. 2.11. We add the simulated defect to the customer's original digital content image. Then in the psychophysical experiment as shown in Fig. 2.12, we ask the subjects to mark the banding according to their observations based on the subject guiding rulers on the bottom of the GUI to get subject marked images $S[m, n]$. Again, to be more clear, we have three markers: *red* stands for strong banding which is the most visible banding; *yellow* stands for

Table 2.2
Incorrect count in percentage (%) of the record from subjects participate in experiment without rulers.

| Sti \ Sub | 1 | 2 | 3 | 4 | 5 | 6 | 7 | 8 | 9 | 10 | Mean (Sub) | Std (Sub) |
|---|---|---|---|---|---|---|---|---|---|---|---|---|
| 1 | 27.8 | 47.2 | 33.3 | 41.7 | 30.6 | 44.4 | 41.7 | 44.4 | 36.1 | 25 | 37.2 | 7.8 |
| 2 | 22.2 | 36.1 | 30.6 | 13.9 | 13.9 | 25 | 58.3 | 30.6 | 27.8 | 25 | 28.3 | 12.7 |
| 3 | 22.2 | 27.8 | 25 | 13.9 | 19.4 | 25 | 22.2 | 27.8 | 22.2 | 30.6 | 23.6 | 4.8 |
| 4 | 19.4 | 30.6 | 38.9 | 13.9 | 27.8 | 41.7 | 50 | 38.9 | 36.1 | 50 | 34.7 | 11.9 |
| 5 | 25 | 38.9 | 41.7 | 47.2 | 19.4 | 41.7 | 36.1 | 50 | 44.4 | 41.7 | 38.6 | 9.6 |
| 6 | 38.9 | 33.3 | 38.9 | 38.9 | 25 | 25 | 33.3 | 33.3 | 36.1 | 22.2 | 32.5 | 6.3 |
| Mean(Sti) | 25.9 | 35.6 | 34.7 | 28.2 | 22.7 | 33.8 | 40.3 | 37.5 | 33.8 | 32.4 | / | / |
| Std(Sti) | 6.9 | 6.9 | 6.3 | 15.9 | 6.2 | 9.7 | 12.8 | 8.6 | 7.7 | 11.1 | / | / |

medium banding; and *green* stands for weak banding which is the least visible banding. Regions without marks mean there is no visible banding there. After a series of processing steps, we get the modified ground truth data (MGTI) $G_M[m, n]$ for the training process which is shown in Sec. 3.3, Fig. 3.12. The process for developing the simulated defects and incorporating them within the customers' content to get the stimuli is described in Ref. [55]. The original design of the GUI, and the customer's original digital content image used in our psychophysical experiments to assess the visibility of banding in the presence of customer content is similar as it is described in Ref. [60]. All the content shown in original digital content image are obtained on the Purdue University website.

The experiment setup is described as follow:

1. One expert subjects participated in this experiment.

3. One monitor with the same setup as the detection and discrimination experiment.

4. Twenty stimuli are shown in the interface randomly.

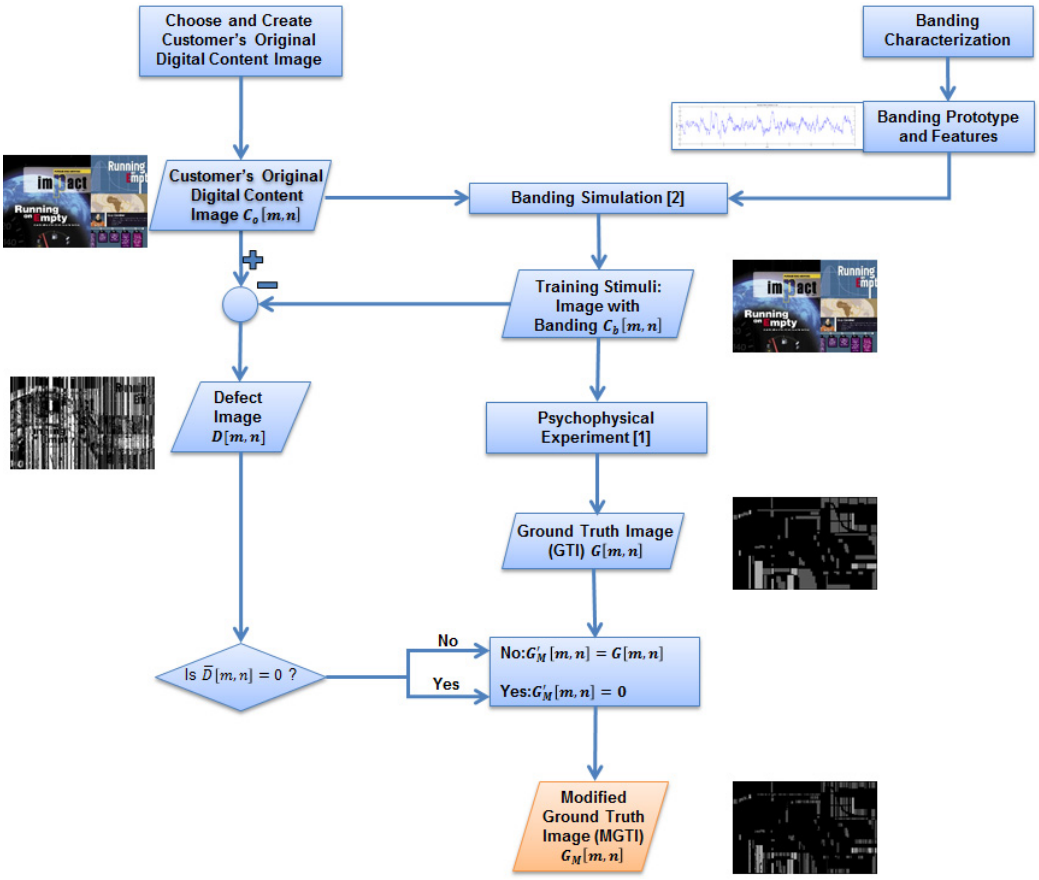


Fig. 2.11. Scenario for generating customer's original digital content image, defect image, and the modified ground truth image for training the MMDVP.

5. Subject guiding rulers in three different levels are shown on the bottom of the GUI.

6. Step-wedge is used in a vertical direction on both sides of the GUI in the same way as the subjects guiding rulers validation experiments.

7. Subjects can choose between three severity levels with different color of the marker and draw rectangular mark on the stimuli in the same way as the subjects guiding rulers validation experiments.

The ground truth image (GTI) $G[m,n]$ has four levels: the areas with *red* mark are integer 9 (JND); areas with *yellow* mark are integer 6 (JND); areas with *green* mark are integer 3 (JND); and finally the regions without marks are integer 0. To get

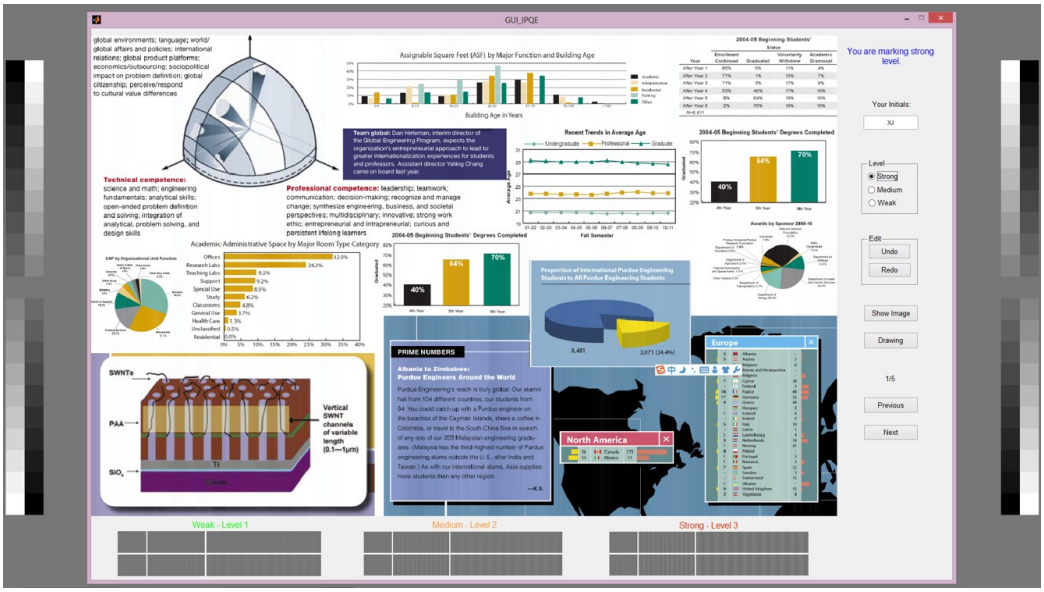


Fig. 2.12. Example stimulus with natural image content on GUI, which is used in psychophysical experiment for collecting modified ground truth data.

the MGTI $G_M[m,n]$, first we get the defect image by subtracting the stimulus with defect from the customer's original digital content image, then take absolute value of it. Second, we need to pick up the value of those pixels in the GTI, which do not have a zero value in the defect image $D[m,n]$. After this series of processing steps, we get the modified ground truth information for the training process.

## 2.3 Discussion and Conclusion

We used to train our parameters on the GTI directly. After observing the PDVI results, we notice that there are regions, which our model predict as with banding actually do not have banding. The reason is that the subject used a rectangle marker to mark the banding (See Fig. 2.13 for a better vision) in the psychophysical experiment. Then the marker will cover the whole region even there might has no banding at all. Therefore, the GTI will capture the regions with no banding by mistake. By masking the defect image (See Fig. 2.15) we can prevent the regions that subject

marked as banding areas, which actually do not contain banding. Then MGTI (See Fig. 2.16) will take out the regions marked as visible banding that actually do not have banding, thus providing us a more accurate modified ground truth data. We also calculate the root mean square JND of the modified ground truth images on the marked region. We can see in Fig. 2.17, the average JND around 3.7 which is close to the weak level of banding. This is the reality of the banding on natural images.


Fig. 2.13. Example of subject marked image.

Fig. 2.14. Example of ground truth image.

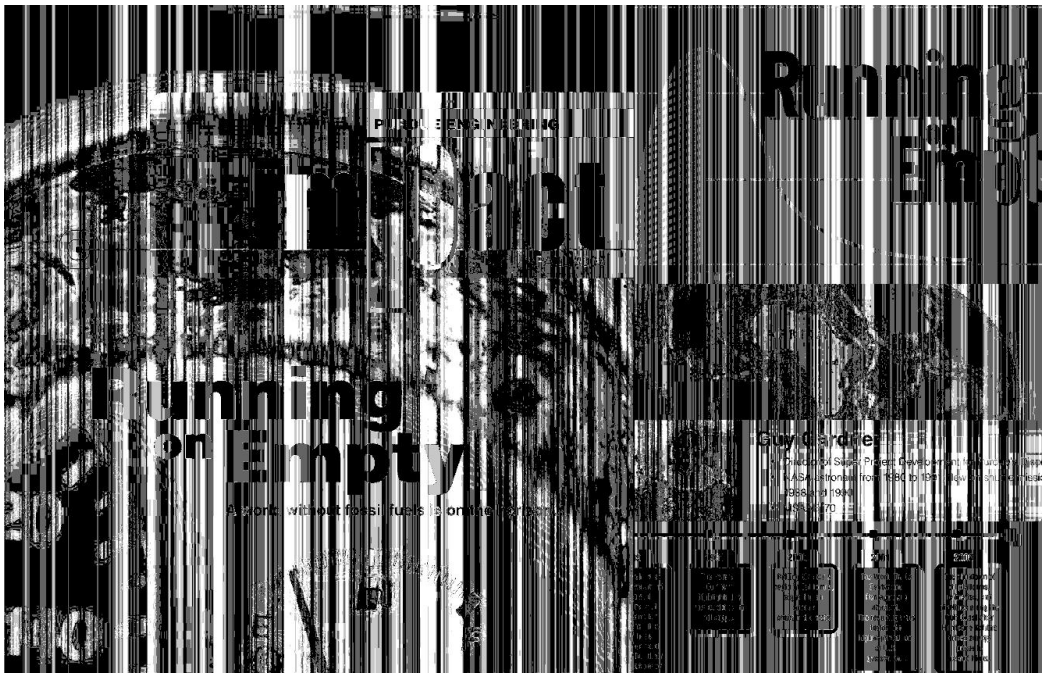

Fig. 2.15. Example of defect image.

Fig. 2.16. Example of modified ground truth image.

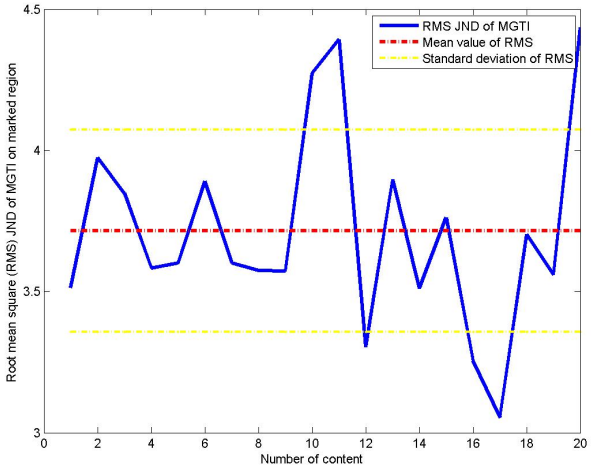


Fig. 2.17. Root mean square JND of the twenty modified ground truth images.

# 3. MASKING MEDIATED PRINT DEFECT VISIBILITY PREDICTOR METHODOLOGY

## 3.1 Method Background

In this section, we explain the overall structure, features, and prediction framework of the MMPDVP in detail. Our predictor structure and training approach draw upon some of the ideas previously used to develop the Optimal Unsharp Mask (OUM) [61] and the Adaptive Bilateral Filter (ABF) [62]. The method is called pixel classification algorithm which is based on the Laplacian of Gaussian (LoG) operator. By filtering the input image with the LoG kernel one can get a high-pass filtered output image. Then each pixel of the output image will be classified to an integer value. Finally, a classification map is obtained as a feature for the model. Although, we are not using the LoG operator, we use four quantizers to get our classification maps for our MMPDVP.

## 3.2 Structure of Masking Mediated Defect Visibility Predictor

Figure 3.1 shows the detailed framework for the MMPDVP. There are four features in this MMPDVP model. As we described above, the idea are similar as which Sang Ho and Buyue used in OUM and ABF [61, 62]. The four features are quantized into certain levels to get the classification index images. The four index images, the texture likelihood index image $t[m, n]$, the uniform salience-object index image $u[m, n]$, the quantized color index image $q_c[m, n]$, and the banding visibility index image $b[m, n]$. We will discuss the four features in more detail in 3.2.1. Some of the features are processed in $CIE\ L^*a^*b^*$ space. We convert from $sRGB$ space into $CIE\ XYZ$ space, then further convert the image from $CIE\ XYZ$ space into $CIE\ L^*a^*b^*$ space.

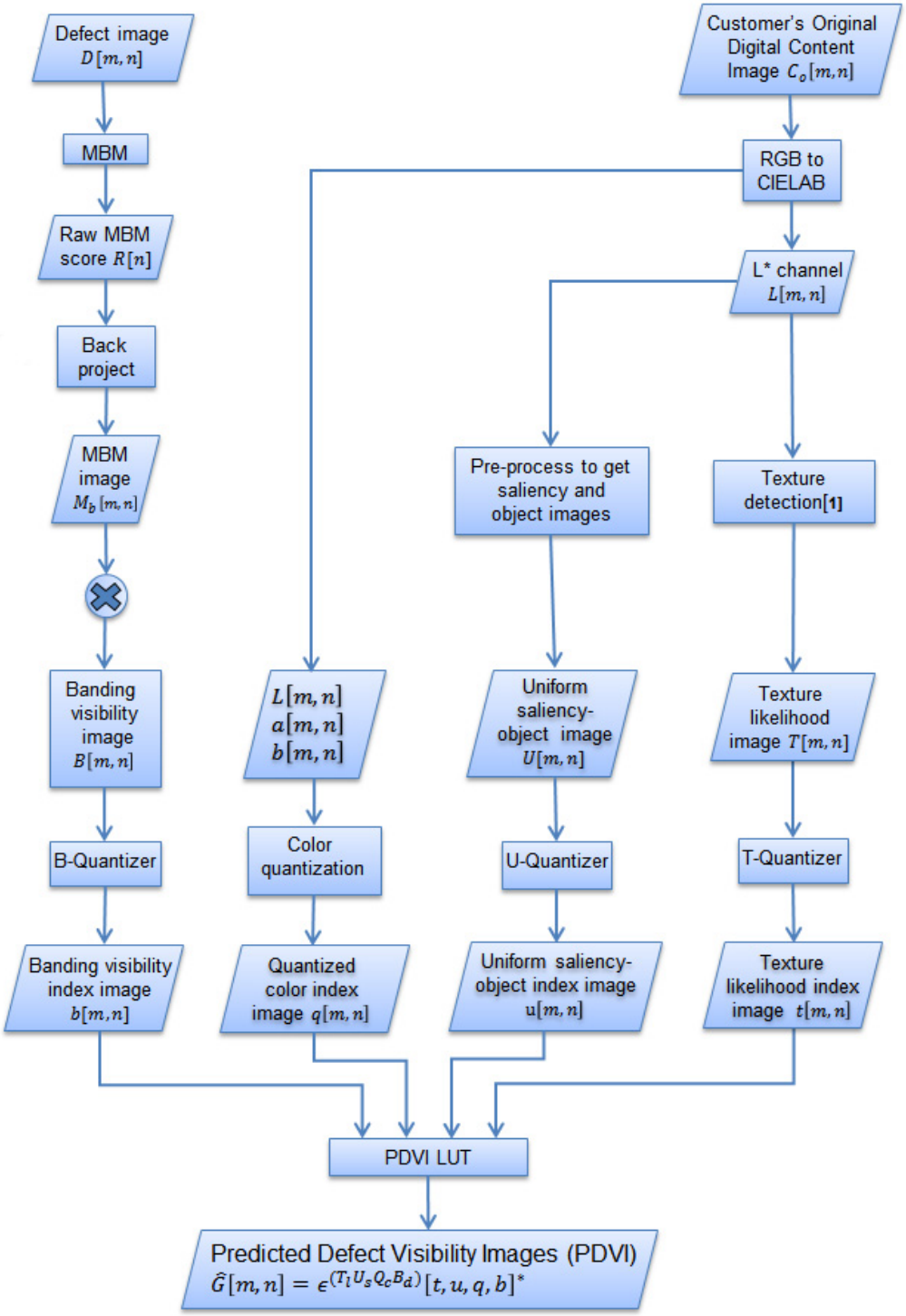


Fig. 3.1. Detailed framework for the MMPDVP.

### 3.2.1 Four features used in MMPDVP

The four features, the texture likelihood index image $t[m,n]$, the uniform salience-object index image $u[m,n]$, the quantized color index image $q_c[m,n]$, and the banding visibility index image $b[m,n]$ are obtained from the texture likelihood image $T_l[m,n]$, the uniform salience-object image $U_s[m,n]$, the color image in $L^*a^*b^*$ space, and the banding visibility image $B_d[m,n]$, respectively.

#### 3.2.1.1 For the texture likelihood index image $t[m,n]$.

To get the texture likelihood image $T_l[m,n]$, we use the method that described in Ref. [63]. This algorithm detects the texture regions based on component counts, and use Block Truncation Coding (BTC) [64] as the clustering method. We compute the texture likelihood image from the $L^*$ channel of the customer's original digital content image $C_o[m,n]$. The texture likelihood image $T_l[m,n]$ can provide the information about how the image content masks the defect. It can show the high frequency regions such as the text areas shown in Fig. 3.3. Then $T_l[m,n]$ is quantized by a certain level quantizer to get the texture likelihood index image $t[m,n]$.

The $T$-quantizer is given by

$$\begin{aligned} t\left[m,n\right] &= Q^{(T_l)}\left(T_l\left[m,n\right]\right) \\ &= \begin{cases} \lfloor \breve{T}_l\left[m,n\right] \rfloor, & 0 \leq \breve{T}_l\left[m,n\right] < T, \\ T-1, & \breve{T}_l\left[m,n\right] = T, \end{cases} \end{aligned} \tag{3.1}$$

and

$$\breve{T}_l\left[m,n\right] = T\frac{T_l\left[m,n\right] - min\left(T_l\left[m,n\right]\right)}{max\left(T_l\left[m,n\right]\right) - min\left(T_l\left[m,n\right]\right)}. \tag{3.2}$$

Here $\lfloor x \rfloor$ denotes flooring $x$ to the nearest integer that is less than or equal to $x$. $T$ is the quantization level for $T$-quantizer.


Fig. 3.2. Example of customer's original content image.

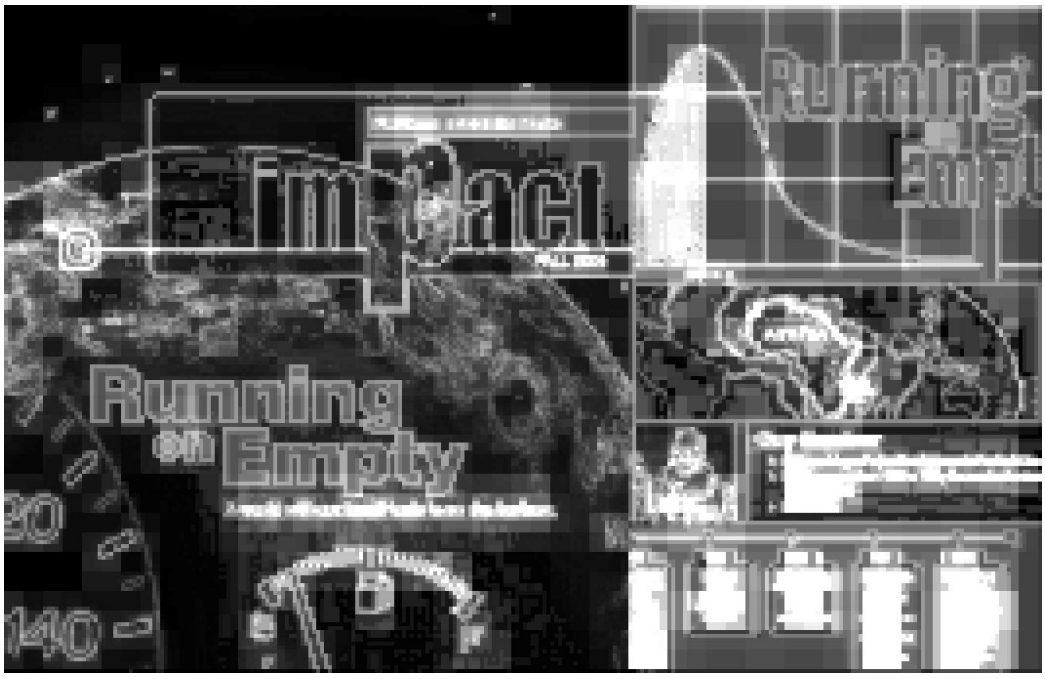

Fig. 3.3. Example of texture likelihood image.

#### 3.2.1.2 For the uniform salience-object index image $u[m, n]$.

Figure 3.4 shows the framework for getting the uniform salience-object image $U_s[m, n]$. The input is the customer's original digital content image in $CIE\ L^*a^*b^*$ space. On one hand, we segment the input by Gaussian Mixture Models (GMM) with Bayesian Information Criteria (BIC) to get the object map [65]. On the other hand, we use a salience measure algorithm described in reference [66] to get the salience map. We then clean up the small regions in the object map and combine it with the salience map. Finally, we get an uniform salience-object image. This uniform salience-object image will provide us a uniform value about how salient of each segment. We assume the salient regions will expose the banding in those areas. Figure 3.5 shows an example of the uniform salience-object image. Then the uniform salience-object image $U_s[m, n]$ is quantized by a certain level quantizer to get the uniform salience-object index image $u[m, n]$.

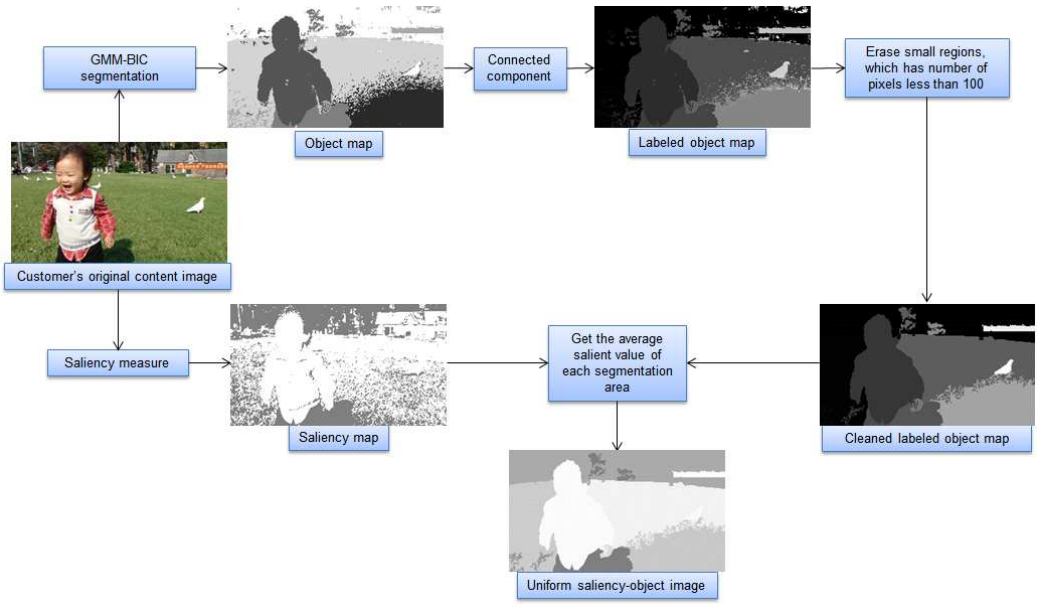


Fig. 3.4. Application for getting uniform salience-object image.


Fig. 3.5. Example of uniform salience-object image.

The $U$-quantizer is given by

$$\begin{aligned} u\left[m,n\right] &= Q^{(U_s)}\left(U_s\left[m,n\right]\right) \\ &= \begin{cases} \lfloor \breve{U}_s\left[m,n\right] \rfloor, & 0 \leq \breve{U}_s\left[m,n\right] < U, \\ U-1, & \breve{U}_s\left[m,n\right] = U, \end{cases} \end{aligned} \tag{3.3}$$

and

$$\breve{U}_s\left[m,n\right] = U \frac{U_s\left[m,n\right] - min\left(U_s\left[m,n\right]\right)}{max\left(U_s\left[m,n\right]\right) - min\left(U_s\left[m,n\right]\right)}. \tag{3.4}$$

Here $U$ is the quantization level for $U$-quantizer.

#### 3.2.1.3 For the quantized color index image $q[m,n]$.

To obtain the quantized color index image $q[m,n]$, we use the customer's original digital content image in $L^*a^*b^*$ space as input. The values in the three channels of each pixel work as a 3-D feature vector. We then use $K$-means clustering to classify the color image into a index image $q[m,n]$ with the expected quantization level.


Fig. 3.6. Example of quantized color index image.

#### 3.2.1.4 For the banding visibility index image $b[m, n]$.


Fig. 3.7. Overview of MBM.

To obtain the banding visibility index image $b[m, n]$, we first get the defect image $D[m, n]$ by subtracting the customer's original digital content image $C_o[m, n]$ from the printed image with banding $C_b[m, n]$. We then take the absolute value of $D[m, n]$ as the input to Hila's Mechanical Band Measurement (MBM) tool [28]. Figure 3.7 shows an overview of the MBM tool. First, one need to get the printout of the test job from HP Indigo Press, then scan the printout. Most of the time, this MBM tool

will take a scanned gray-scale printout with mechanical bands as input, and finally provide a 1-D score that correlates with band severity as output.

As shown in Fig. 3.1, after we get the raw MBM score $R[n]$ (See Fig. 3.8 for a better vision), we back projected this 1-D score to get a 2-D image called back projected MBM image $M_b[m, n]$ (See Fig. 3.9) which has the constant banding along the vertical direction. We multiply this $M_b[m, n]$ by $D[m, n]$ (See Fig. 3.10) to get a modulated MBM image $B[m, n]$ (See Fig. 3.11), which predicts how the subjects will see a defect in a gray scale image.

One may argue that why we are not just quantizing the back projected MBM image $M_b[m, n]$ to get the banding visibility index image $b[m, n]$. Notice the defect image $D[m, n]$ in Fig. 3.10 has some dark regions in the image. The defect image $D[m, n]$ has a very different form compare to the back projected MBM image $M_b[m, n]$. The banding profile in $M_b[m, n]$ is just a back project from the 1-D score. The banding is constant along the vertical direction, but the defect image $D[m, n]$ is not. The dark region in $D[m, n]$ is caused by the color space dependence. By multiplying $M_b[m, n]$ by the $D[m, n]$, our defect image modulated MBM $B[m, n]$ can accurately chapter the character of the defect to what the subjects observe.

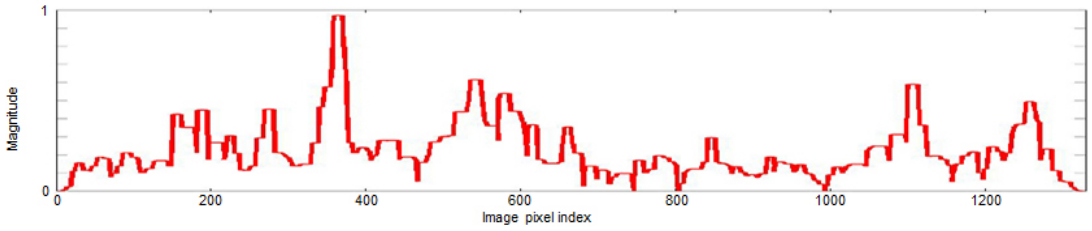


Fig. 3.8. Example of raw MBM score.

We use the same method as the previous two images to get the banding visibility index image $b[m, n]$.

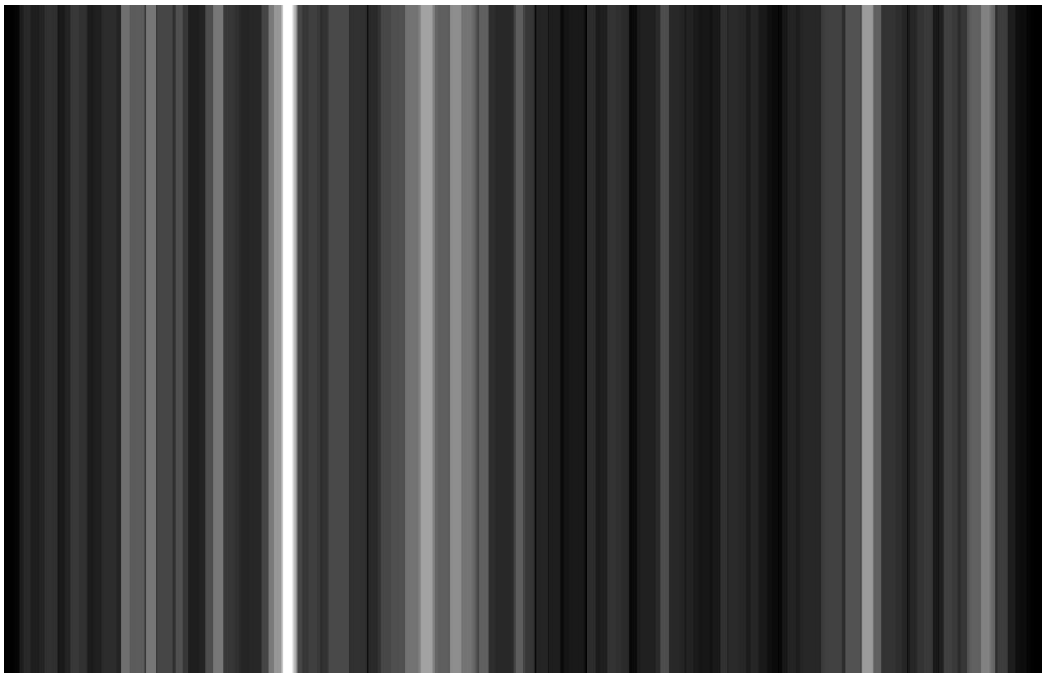

Fig. 3.9. Example of back projected MBM image.

Fig. 3.10. Example of defect image.

Fig. 3.11. Example of modulated MBM image.

The $B$-quantizer given by

$$\begin{aligned} b[m,n] &= Q^{(B_d)}(B_d[m,n]) \\ &= \begin{cases} \lceil \breve{B}_d[m,n] \rceil, & 0 \le \breve{B}_d[m,n] < B, \\ B-1, & \breve{B}_d[m,n] = B, \end{cases} \end{aligned} \tag{3.5}$$

and

$$\breve{B}_d[m,n] = B \frac{B_d[m,n] - min(B_d[m,n])}{max(B_d[m,n]) - min(B_d[m,n])}. \tag{3.6}$$

Here $\lceil x \rceil$ denotes ceiling $x$ to the nearest integer that is more than or equal to $x$. $B$ is the quantization level for $B$-quantizer.

The texture likelihood image accounts for the image content masking effect, the uniform salience-object image accounts for the banding weight in each segment, the quantized color image accounts for the color dependence of defect visibility, and the defect visibility image provides the defect information. The impact of these four features on overall defect visibility is summarized by four quantized index images, which are analogous to segmentation images. The predicted defect visibility is chosen

independently for each different combination of quantizer output levels. For each such combination, the predicted defect visibility is stored as a parameter in the PDVI Look-Up Table (LUT). By training these quantized images to the modified ground truth information, we can optimize the parameters, and better predict how the subjects observe the defects in a specific region. For the record, we always use $T = U = Q_c = B$ in this work.

### 3.2.2 Predictor structure

The predictor is simply a 4-D LUT that yields an identical prediction for all occurrences of the same four-tuple of values from the four index images. To specify its structure, we define the different regions of each quantization level in our index images according to

$$\Omega_{t_0}^{(T_l)} = \left\{[m,n] : t\left[m,n\right] = t_0\right\}, 0 \leq t_0 \leq T-1, \tag{3.7}$$

$$\Omega_{u_0}^{(U_s)} = \left\{[m,n] : u\left[m,n\right] = u_0\right\}, 0 \leq u_0 \leq U-1, \tag{3.8}$$

$$\Omega_{q_(c0)}^{(Q_c)} = \left\{[m,n] : q_c\left[m,n\right] = q_(c0)\right\}, 0 \leq q_(c0) \leq Q_c-1, \tag{3.9}$$

$$\Omega_{b_0}^{(B_d)} = \left\{[m,n] : b\left[m,n\right] = b_0\right\}, 0 \leq b_0 \leq B-1. \tag{3.10}$$

All the pixels with the same quantization level are in the same segment region. These regions will be used in Sec. 3.3 for the training and testing processes. Then the PDVI result is defined as

$$\hat{G}\left[m,n\right] = \epsilon^{(T_l U_s Q_c B_d)}\left[t\left[m,n\right], u\left[m,n\right], q_c\left[m,n\right], b\left[m,n\right]\right]. \tag{3.11}$$

Having explained the structure of our predictor, we will next introduce in Sec. 3.3 how we train the set of free parameters to the modified ground truth information.

## 3.3 Training and Testing Process

### 3.3.1 Training the parameters on the modified ground truth information

Once we finish the step of converting the subject marked image $S[m,n]$ to the MGTI $G_M[m,n]$, we then train the parameters on the modified ground truth information to get the optimized parameters for our MMPDVP. Figure 3.12 shows the training process for the MMPDVP. After generating the customer's original digital content image and defect image, we use these two images as input to the MMPDVP with free parameters. We then calculate the cost function, which penalizes the difference between the output PDVI of the MMPDVP and the modified ground truth data.

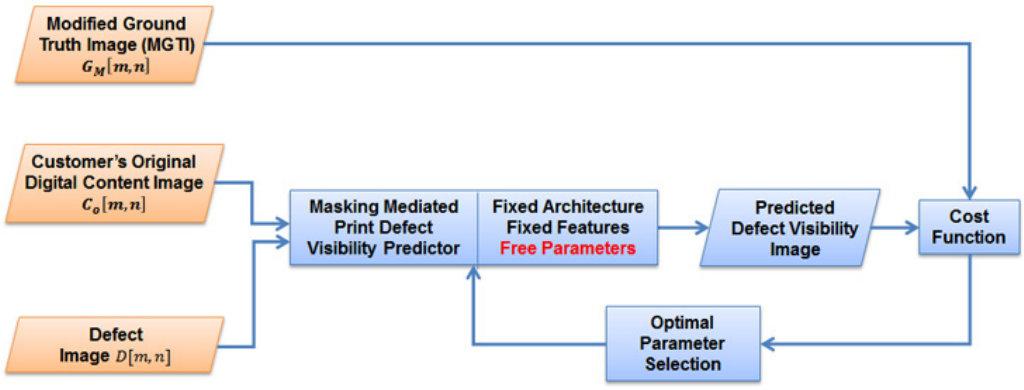


Fig. 3.12. Framework for MMPDVP training process. We calculate the cost function, which penalizes the difference between the output PDVI of the MMPDVP and the modified ground truth data. We minimize this cost function to get the optimized parameters.

We define the cost function

$$\phi = \sum_{i=0}^{I-1}\sum_{t=0}^{T-1}\sum_{u=0}^{U-1}\sum_{q_c=0}^{Q_c-1}\sum_{b=0}^{B-1}\sum_{[m,n]\in {}^{i}\Omega_{t,u,q_c,b}^{(T_l U_s Q_c B_d)}} \left| {}^{i}\hat{G}\,[m,n] - {}^{i}G_M\,[m,n] \right|^2, \tag{3.12}$$

as the total squared error between the predicted and actual ground truth. Here the parameter $i$ indexes the results for the individual modified ground truth images used for the training and $I$ is the total number of such images used for training.

The regions $\Omega_{t_0}^{(T_l)}$, $\Omega_{u_0}^{(U_s)}$, $\Omega_{q_c 0}^{(Q_c)}$, and $\Omega_{b_0}^{(B_d)}$ are defined by Eqs. (3.7) -(3.10). For each region with a different combination of values for $t$, $u$, $q_c$, and $b$, we calculate the total squared error between the MGTI and the PDVI.

By minimizing the cost function, we get the optimized parameters $\epsilon_{OPT}^{(T_l U_s Q_c B_d)}[t, u, q_c, b]$ as

$$\epsilon_{OPT}^{(T_l U_s Q_c B_d)}[t, u, q_c, b] = \frac{\sum_{i=0}^{I-1} \sum_{[m,n] \in {}^i\Omega_{t,u,q_c,b}^{(T_l U_s Q_c B_d)}} {}^iG_M[m, n]}{\sum_{i=0}^{I-1} \sum_{[m,n] \in {}^i\Omega_{t,u,q_c,b}^{(T_l U_s Q_c B_d)}} 1}, \tag{3.13}$$

which is the conditional mean of $G_M[m, n]$, given the four-tuple value $[t, u, q_c, b]$ for the three index images. We then store these optimized parameters $\epsilon_{OPT}^{(T_l U_s Q_c B_d)}[t, u, q_c, b]$ in the PDVI LUT.

### 3.3.2 Training results

We use the optimized parameters, which are stored in the PDVI LUT to get the PDVI training results. We use twenty customer's original digital content images, then apply twenty banding prototypes on these original content images, respectively, to get twenty different stimuli. These are then marked by subject to yield a total of twenty unique standard subject-marked images for training and/or testing. We choose to use nineteen images in Eqs. (3.12) and (3.13) for training and one for testing purposes. We will show the training PDVI result for $T = U = Q_c = B = 8$ quantization levels as an example. Since quantization level 4 is under-fitting, and quantization level 16 is over-fitting. Figure 3.13 - Fig. 3.15 show an example stimulus that is generated with one customer's original digital content image with one banding prototype, subject marked image, and the PDVI training result for that stimulus.

Our subject marked image does not mark the top black region shown in Fig. 3.14. However, our PDVI training result shown in Fig. 3.15 do have low response in that


Fig. 3.13. Example stimulus (customer's original digital content image with one banding prototype).


Fig. 3.14. Subject marked image on the same stimulus to compare with Fig. 3.15.

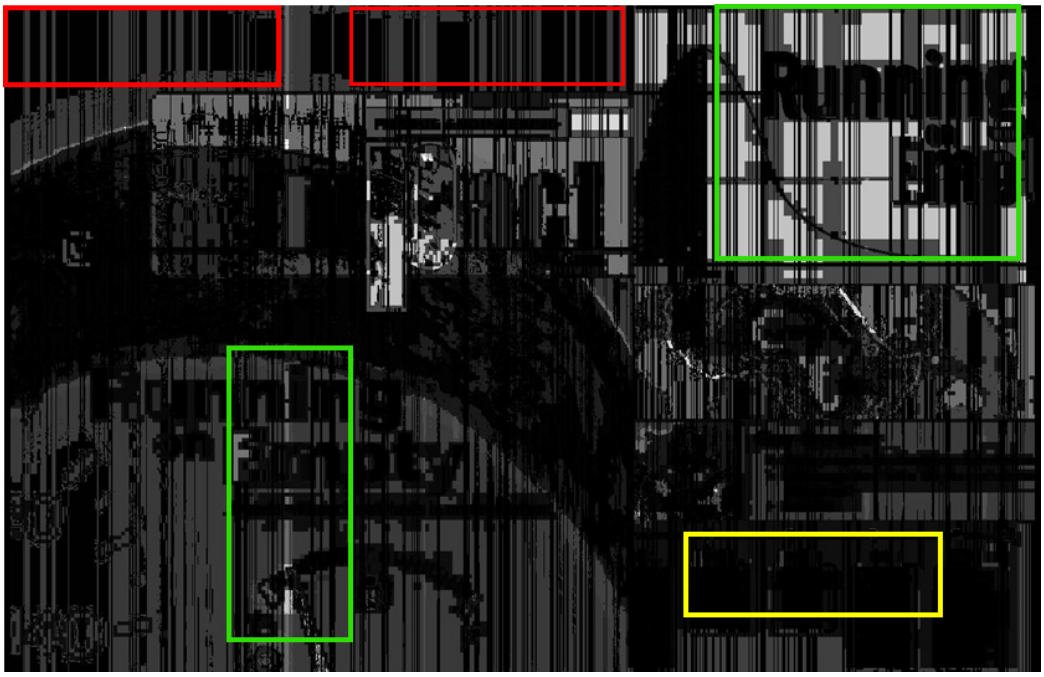

Fig. 3.15. PDVI training result for $T = U = Q_c = B = 8$ quantization levels.

region, which is highlighted in red boxes. And after we check the stimuli, there do have some low level banding in the top black region. This can be a sign that we need to be more careful for getting the subject marked image. Furthermore, we observe that in the region which is highlighted in yellow boxes, where the stimulus has text or high frequency texture, which will masked the banding. The subjects didn't mark anything, and the PDVI training results also didn't have any response. For those regions subjects marked as *yellow* and *green*, the PDVI training result do have response, such as the region which is highlighted in the green boxes.

### 3.3.3 Testing process and error measure

The testing process is similar to the training process. The key elements are the input testing stimulus set and the parameters of the MMPDVP. The testing stimulus set consists of three-tuples of images. Each three-tuple contains the customer's original digital content image, a simulation of the banding that would have appeared on

that content if the document had been printed with the target digital press, and the subject-marked version of that simulated print.

The parameters of the MMPDVP are assumed to have been optimized according to the procedure described in the preceding section. To test our model's accuracy, we calculate

$$e = \sqrt{\frac{1}{I}\sum_{i=0}^{I-1}\frac{1}{N}\sum_{[m,n]\in {}^{i}\Omega_{t,u,q_c,b}^{(T_l U_s Q_c B_d)}}\left|{}^{i}\hat{G}\left[m,n\right]-{}^{i}G_M\left[m,n\right]\right|^2}, \tag{3.14}$$

which is the root mean squared error in JND between the PDVI result and the MGTI marked by the subject on the stimulus. Here $N$ is the total number of the pixels in each image and $I$ is the total number of modified ground truth images used for testing.

### 3.3.4 Testing results

We use the optimized parameters, which are stored in the PDVI LUT to get the PDVI testing result. We show testing result on one stimulus. We use nine images in Eqs. (3.12) and (3.13) for training and one for testing purposes.

From Fig. 3.16 and Fig. 3.17, we can observe that the PDVI test result capture most of the banding compare with the subject marked image. However, there is still room for PDVI to improve on separating the severity levels based on the subject marked image.

### 3.3.5 Cross-validation

We compare the PDVI result on quantization level 8 with a scaled inverse version of SSIM image and a scaled normalized inverse version of pixel-wise Signal-to-Noise Ratio (SNR) image. Figure 3.18 and Fig. 3.19 show their example result on the same content, respectively. We can observe that MMPDVP do a better job on defining the severity level of banding in dark region. To test the accuracy of our MMPDVP quantization level 8, we do a leave-one out cross-validation. Figure 3.20 shows the mean error and standard deviation in JND from cross validation for all the three


Fig. 3.16. Subject marked image on the same stimulus to compare with Fig. 3.17 - Fig. 3.19.

Fig. 3.17. PDVI testing result for $T = U = Q_c = B = 8$ quantization levels.

methods, we can observe that the MMPDVP quantization level 8 has the lowest mean error and standard deviation.

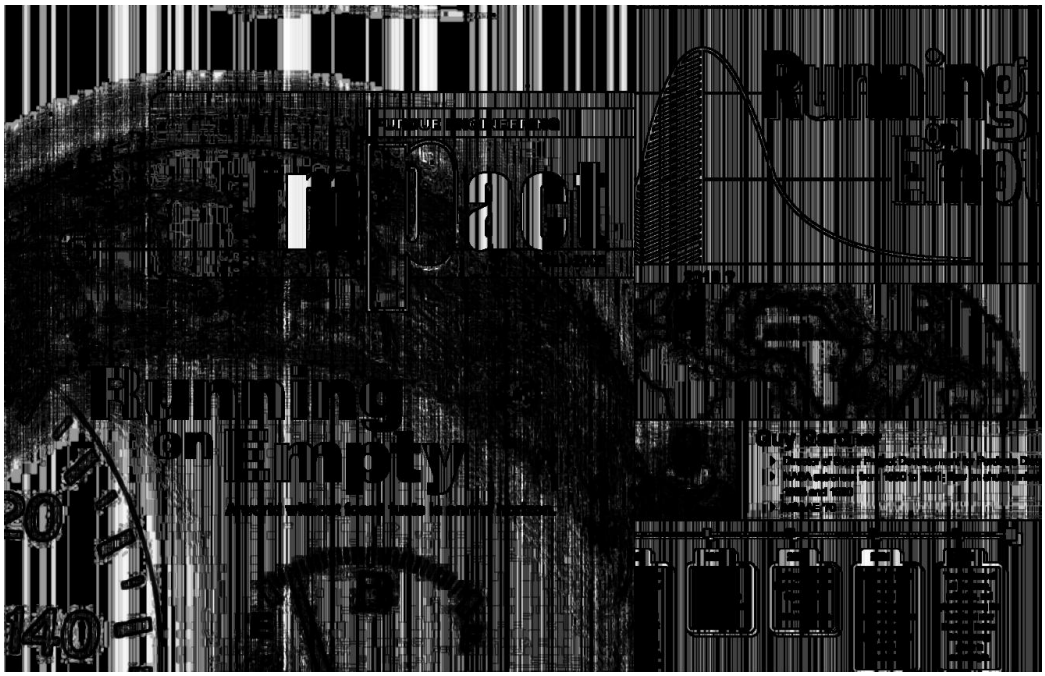

Fig. 3.18. Scaled inverse SSIM

## 3.4 Conclusion

We develop a full-reference predictor for print quality defects generated by a high-end digital press. The predictor is intended to take as input the customer's original digital content and a scanned version of the final printed version of that content [67]. It generates an image map that at each pixel predicts the defect visibility there. Two important aspects of our predictor are that it considers the masking effect of the customer content on defect visibility, and it is trained offline from subject-marked images of typical defects on typical customer content. The prediction is based on four features: local texture, saliency-object image, color quantiztion, and visually-weighted defect strength. The predictor structure is a simple look-up table with the quantized feature images as input. This allows ease of implementation and flexibility


Fig. 3.19. Scaled normalized inverse pixel-wise SNR.

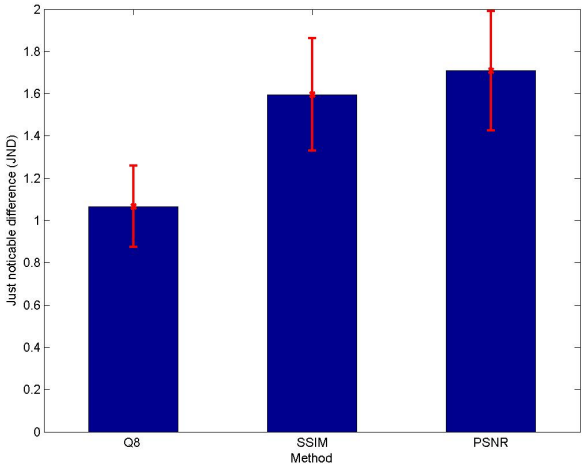


Fig. 3.20. mean error and standard deviation in JND from cross validation for quantization level 8, scaled inverse SSIM, and scaled normalized inverse pixel-wise SNR.

in capturing the nuances of the input and training data. In this work, we consider only the defect of banding that is orthogonal to the process direction of the digital press. Our results show promise for this overall approach to content-mediated print defect visibility prediction.

# 4. A GENERAL APPROACH FOR ASSESSMENT OF PRINT QUALITY

## 4.1 Introduction

Laser Electro-Photographic (EP) printing devices are complex systems, for which the quality of printed documents results from the combination of a large number of factors. For instance, the performance of the print engine, print cartridge, fuser, and other system components can affect the Print Quality (PQ) in numerous aspects, and cause various artifacts.

Several common PQ artifacts that are well studied. Take banding as an example. It is primarily caused by the fluctuations in the angular velocity of the Optical Photo-Conductor (OPC) drum. Most of the time, banding exhibits quasiperiodic variation with medium to low frequency along the process direction. A similar artifact is jitter, except that this artifact has much higher frequency content. Together with repetitive pitch bands, impulse bands, and streaks, all these artifacts are directional. Wavelet-based approaches that extract one artifact and filter out others are well-suited for analysis of such directional artifacts [33, 36–38, 68]. They may not be so well-suited for analysis of PQ defects, such as graininess [37] or mottle that lack strong directionality, or PQ defects that are highly localized, such as spots. Determining the perceptibility and acceptable levels of specific directional defects is quite important. To address this problem, visual inspection, which factors in human perception, has been conducted by examination of actual printed samples [28, 33, 36–38, 68–70] or by softcopy inspection of images that contain simulated print quality defects [23–25]. Other works provide a spatial visualization tool [27], and consider the masking effect of print document content [19] on banding. There are also papers that concentrate

on specific PQ defects, such as ghosting [68], toner scatter [35], and tire marks [71] in EP printing systems.

The approaches discussed above for detecting and assessing PQ defects largely focus on one kind of artifact. However, real print documents can have numerous artifacts present at the same time, as shown in Fig. 4.1. Here we see two spots, one dark and one light highlighted in black boxes, an impulse band/streak indicated by the black arrow, and strong large-area nonuniformity artifacts at the top and bottom edges of the page. There is also not very visible jitter along the vertical direction in the background. Therefore, what is needed is one general approach that can detect artifacts with or without specific directional orientation. The work conducted by the INCITS W1.1 macro-uniformity team [69, 70, 72, 73] on developing methods for assessing macro-uniformity is a step in this direction; but it does not provide a spatial map that identifies specific PQ defects on the page.

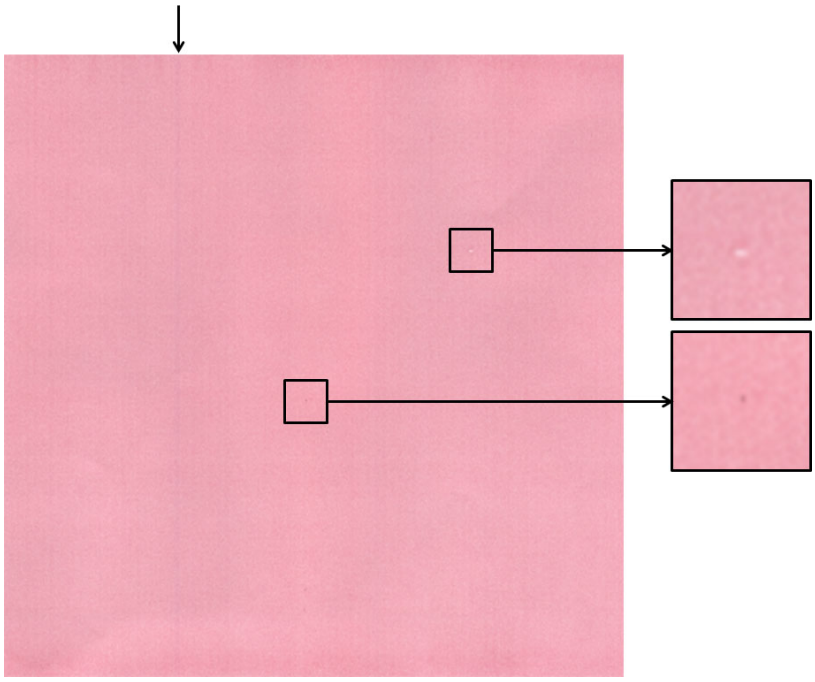

Fig. 4.1. An example print document with multiple artifacts.

In this chapter, we develop an image processing and analysis pipeline that takes as its input a reference digital image and the printed and scanned version of that digital image, and generates an output image that displays a map of the significant defects in the printed image. The analysis is based on two major components: the Structural Similarity (SSIM) index [20,74] and the difference between the digital reference image and the printed and scanned image.

The remainder of this chapter is organized as follows. Section 4.2 introduces the proposed image processing and analysis pipeline. Section 4.3 provides the experimental results, and Section 4.4 contains conclusions and future work.

## 4.2 Proposed Image Processing and Analysis Pipeline

We describe one major algorithm in detail as the fundamental structure of our approach. This algorithm works on uniform test pages with dark and light banding, streaks, bands, spots, and other defects, as well. As shown in Fig. 4.2, there are two inputs to this whole process. One is the master image or reference image $R_{rgb}[m,n]$. The other one is the scanned image $S_{rgb}[m,n]$. Both images are in $sRGB$ color space. Both $R_{rgb}[m,n]$ and $S_{rgb}[m,n]$ are inputs to the image analysis algorithm, which provides a spatial visualization of the detected artifacts, as well as some statistics and metrics. All the results from the image analysis are stored in a database for further use.

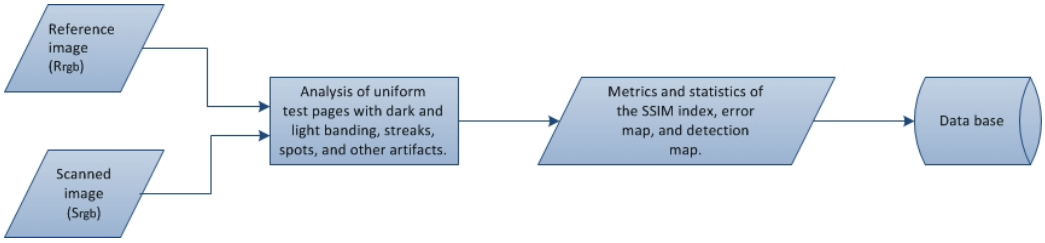


Fig. 4.2. Fundamental structure of proposed image processing and analysis pipeline.

The analysis is based on three major elements: the SSIM index image $I[m,n]$, the error map $E[m,n]$, and the detection map $D[m,n]$. The basic approach is to calculate the SSIM index image $I[m,n]$ and the error map $E[m,n]$ using two different processes, and then to combine them to get a final detection map $D[m,n]$. The main motivation for this approach is that the SSIM index image $I[m,n]$ measurement can effectively find local defects, whereas the error map $E[m,n]$ procedure is better for detecting more distributed defects that cover a larger area of the image. By merging the results from these two very different methods, our analysis can capture the best characteristics of each approach.

Initially, both the reference image and the scanned image are in the $sRGB$ color space. Several preprocessing steps are applied to these images. As shown in Fig. 4.3, we first apply color space conversion from $sRGB$ to $CIE\ L^*a^*b^*$ to the images, then take the $L^*$ channel to get $R_L[m,n]$ and $S_L[m,n]$. After a down-sampling procedure, we obtain the prepared reference image $R[m,n]$ and scanned image $S[m,n]$ at the target resolution. In our work, we use 75 dpi. This completes the preparation of the input information.

### 4.2.1 SSIM index image $I[m,n]$

The SSIM index [20] has become a popular measure for assessing image quality, and has been applied in a wide range of applications. Rather than simply considering the pixel-by-pixel difference between a reference image and a reproduction of that reference, it is based on the computation of three separate measures of local similarity in luminance, contrast, and spatial structure. The version [74] that we use includes a local block matching step that is designed to compensate for local misregistration between the reference image and the reproduction. This is particularly important when the reproduction is obtained by printing and scanning the reference image, due to local non-unformities in spatial scale that can be introduced by the printing and scanning processes.

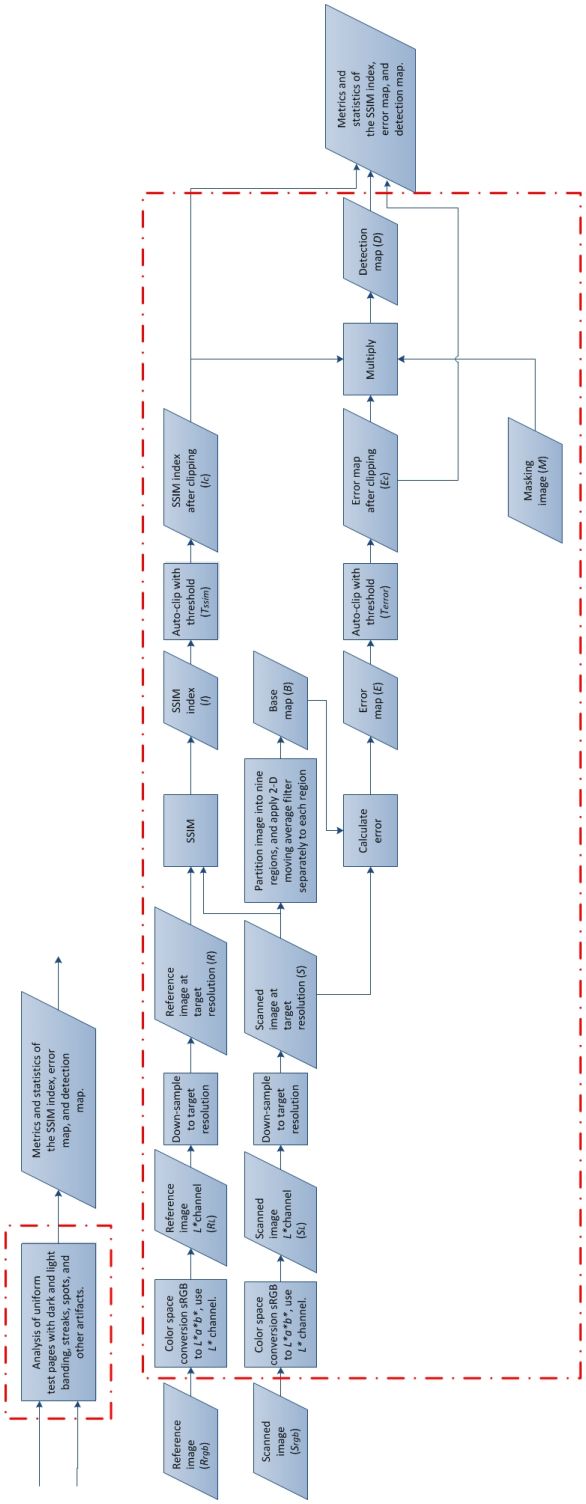


Fig. 4.3. Block diagram of overall image analysis algorithm.

In this chapter, the modified SSIM considers two images $X$ and $Y$. For each pair of image patches $x$ of $X$ and $y$ of $Y$ within a moving Gaussian window, the SSIM score $I(x,y)$ is defined to be

$$I\left(x,y\right)=l\left(x,y\right)\cdot c\left(x,y\right)\cdot s\left(x,y\right), \tag{4.1}$$

where $l$, $c$, and $s$ are the luminance, contrast, and structure components, respectively. This definition of SSIM score is the same as the simplest version of the SSIM score $I\left(x,y\right)=\left[l\left(x,y\right)\right]^{\alpha}\cdot\left[c\left(x,y\right)\right]^{\beta}\cdot\left[s\left(x,y\right)\right]^{\gamma}$ in reference [20], when $\alpha=\beta=\gamma=1$. In reference [74], the definition is modified to be $I\left(x,y\right)=l\left(x,y\right)\cdot c\left(x,y\right)\cdot\frac{1}{2}\big(s\left(x,y\right)+1\big)$, in order to put the SSIM score in the range $[0,1]$.

For the moving Gaussian window, we use a $5\times5$ circularly symmetric Gaussian weighting function $w=\{\omega_i|\,i=1,2,\ldots,N\}$, with standard deviation of 1.5. Then the estimates of the local statistics: weighted mean $\mu_x$, standard deviation $\sigma_x$, and covariance function $\sigma_{xy}$ are defined as

$$\mu_x=\sum_{i=1}^{N}\omega_i x_i, \tag{4.2}$$

$$\sigma_x=\left(\sum_{i=1}^{N}\omega_i\left(x_i-\mu_x\right)^2\right)^{\frac{1}{2}}, \tag{4.3}$$

$$\sigma_{xy}=\sum_{i=1}^{N}\omega_i\left(x_i-\mu_x\right)\left(y_i-\mu_y\right). \tag{4.4}$$

Then we define the $l$, $c$, and $s$ components as follows

$$l\left(x,y\right)=\frac{2\mu_x\mu_y+C_1}{{\mu_x}^2+{\mu_y}^2+C_1}, \tag{4.5}$$

$$c\left(x,y\right)=\frac{2\sigma_x\sigma_y+C_2}{\sigma_x^2+\sigma_y^2+C_2}, \tag{4.6}$$

$$s\left(x,y\right)=\frac{|\sigma_{xy}|+C_3}{\sigma_x\sigma_y+C_3}, \tag{4.7}$$

where $C_1$, $C_2$, and $C_3$ are constants to stabilize the computation. Detailed definitions of these three constants and usage of the three components can be found in reference

[20]. In this chapter, the luminance $l$ and contrast $c$ have exactly the same definition as in references [20, 74]. However, we use the absolute value of $\sigma_{xy}$ in the structure component $s$, which is different from references [20, 74], since we would like the SSIM score to obey the following properties

$$I(x,y) = I(y,x), \tag{4.8}$$

$$I(x,y) \in [0,1], \tag{4.9}$$

$$I(x,y) = 1, \iff x \equiv y. \tag{4.10}$$

In making these modifications, we are following the same three properties in reference [74]. However, unlike reference [74], we use slightly different definitions for the SSIM score $I(x,y)$ $\big($Eq.(4.1)$\big)$ and the structure component $s$ $\big($Eq.(4.7)$\big)$ to achieve the second property. In reference [20], the range of the SSIM score is $[-1,1]$. In this chapter and reference [74] the range of SSIM score is $[0,1]$, where 0 is solid black indicating the worst possible defect, and 1 is solid white indicating that there is no defect.

In this chapter, the inputs to the modified SSIM measurement are the reference image $R[m,n]$ $(X)$ and the scanned image $S[m,n]$ $(Y)$. The SSIM score $I(x,y)$ between images $X$ and $Y$ at each position of the moving Gaussian window forms the the SSIM index image $I[m,n]$ with the same size as that of $R[m,n]$ and $S[m,n]$.

### 4.2.2 Error map $E[m,n]$

To prepare the error map $E[m,n]$, we first need to calculate the base map $B[m,n]$. Figure 4.4 shows a block diagram for this process. We apply one of a set of 2-D moving average filters to each of nine regions of the scanned image $S[m,n]$ defined by the partition shown in Fig. 4.5. A moving average filter with specific window size $[N_{hi}, N_{wi}]$ is applied to the scanned image $S_i[m,n]$ within the $i$-th region, $i = 1, ..., 9$. The dimensions of each region relative to the dimensions of the entire image are

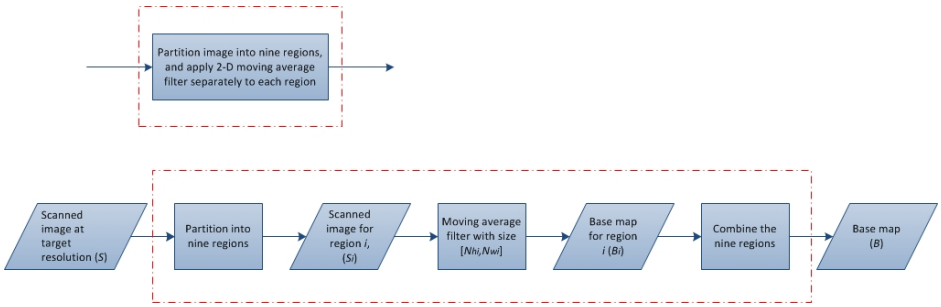


Fig. 4.4. Detailed framework for calculating the base map.

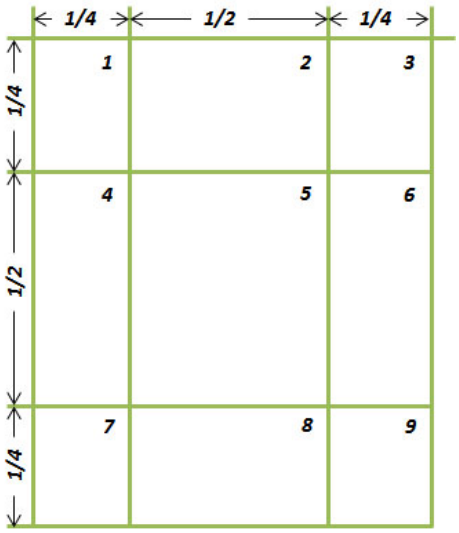


Fig. 4.5. Partitioning of the image into nine regions for the moving average filter step.

indicated by the fractions shown in Fig. 4.5. The filter output from the $i$-th region is given by

$$B_i\left[m,n\right]=f\left(S_i\left[m,n\right],N_{hi},N_{wi}\right). \tag{4.11}$$

Here the function $f\left(\cdot\right)$ is the 2-D moving average filter with window height $N_{hi}$ and width $N_{wi}$ defined as

$$N_{hi}=r\cdot H_i, \tag{4.12}$$

$$N_{wi}=r\cdot W_i, \tag{4.13}$$

where $H_i$ and $W_i$ are the height and width of the $i$-th region. In this chapter, we use the ratio $r = 0.5$.

Finally, we combine the filter outputs $B_i[m,n]$ from all nine regions to form the base map $B[m,n]$. This base map $B[m,n]$ is basically a smoothed version of the scanned image $S[m,n]$. The intent of the moving average filtering operation is to suppress the highest frequency components of the noise, while retaining the spatial structure of the defects. The motivation for partitioning the image into a large center block, smaller blocks along the edges, and even smaller blocks in the four corners, is based on our empirical observation that the spatial scale of the defects also decreases approximately in proportion to the size of these regions. Thus we are eliminating a fixed fraction of the high-frequency content across the entire image.

Once we obtain the base map $B[m,n]$, we then calculate the error map $E[m,n]$ according to

$$E^{'}[m,n] = 100 - \left|S[m,n] - B[m,n]\right|, \tag{4.14}$$

and

$$E[m,n] = \frac{E^{'}[m,n] - \min(E^{'}[m,n])}{\max(E^{'}[m,n]) - \min(E^{'}[m,n])}. \tag{4.15}$$

In Eq.(4.14), we invert the absolute difference between the scanned image $S[m,n]$ and the base map $B[m,n]$. In this way, after normalization, as is the SSIM index image $I[m,n]$, the error map $E[m,n]$ is in the range $[0,1]$, where 0 is solid black indicating the worst possible defect, and 1 is solid white indicating that there is no defect.

### 4.2.3 Detection map $D[m,n]$

Once we get the SSIM index image $I[m,n]$ and error map $E[m,n]$, they need to be clipped according to

$$I_c[m,n] = \begin{cases} 1, & I[m,n] \geqslant T_{ssim} \\ I[m,n], & else \end{cases}, \tag{4.16}$$

and

$$E_c[m,n] = \begin{cases} 1, & E[m,n] \geqslant T_{error} \\ E[m,n], & else \end{cases}. \tag{4.17}$$

Clipping is performed on the SSIM index image $I[m,n]$ and the error map $E[m,n]$ to get rid of most of the mottle in the background. The thresholds $T_{ssim}$ and $T_{error}$ are chosen by calculating the nine regions' statistics of the SSIM index image and the error map, respectively. In this chapter, we use the same partitioning method as shown in Fig. 4.5 to divide the above two images into the nine regions.

By multiplying $I_c[m,n]$ and $E_c[m,n]$ together, we define the detection map $D[m,n]$ as

$$D\left[m,n\right] = I_c\left[m,n\right] \cdot E_c\left[m,n\right] \cdot M\left[m,n\right]. \tag{4.18}$$

Here $M[m,n]$ is a binary mask, which is used to locate the region of interest (ROI). The detection map $D[m,n]$ provides a spatial visualization of the print defects. It is also in the range $[0,1]$. The gray scale of the detection map $D[m,n]$ indicates the severity of the defects, where 0 is solid black indicating the worst possible defect, and 1 is solid white indicating that there is no defect. We first define the inverse percentage coverage of defect pixels $P$ as

$$P = 100 - \frac{\sum\limits_{\substack{[m,n] \\ D[m,n]\neq 1}} 1}{\sum\limits_{[m,n]} M\left[m,n\right]} \times 100\%, \tag{4.19}$$

we then define a score $C$

$$C = \frac{\sum\limits_{\substack{[m,n] \\ D[m,n]\neq 1}} D\left[m,n\right]}{\sum\limits_{\substack{[m,n] \\ D[m,n]\neq 1}} M\left[m,n\right]} \times 100\%, \tag{4.20}$$

as a metric that indicates the total score of the defects over the entire defect region. $P$ and $C$ together will provide the information for the print defect severity, higher $P$ and $C$ indicate better print quality. For example, when $P$ is high and $C$ is low, it indicates that the target print test page appears severe defects which only cover a small amount of regions compare with the whole page.

Running under Windows 7 on a computer with an Intel Core i7-2640 2.80 GHz CPU, the whole process of this approach on a ROI with about $638 \times 825$ pixels takes approximately 5 seconds.

## 4.3 Experimental Results

In this section, we present several experimental results. Figure 4.6 shows the spatial visualization results for the example print document with multiple defects we mentioned at the beginning of this chapter. Figure 4.6(a) is the original scanned image with defects; Fig. 4.6(b) is the detection map; Fig. 4.6(c) is the error map before clipping; Fig. 4.6(d) is the error map after clipping; Fig. 4.6(e) is the SSIM index image before clipping; Fig. 4.6(f) is the SSIM index image after clipping. All the measurement figures from Fig. 4.6(b) - 4.6(f) are in the range $[0, 1]$. The gray value in these images indicates the severity of the defects, where 0 is solid black indicating the worst possible defect, and 1 is solid white indicating that there is no defect.

As shown in Figs. 4.6(a) - 4.6(f), there are two spots, one light and one dark, highlighted by the red circles, an impulse streak highlighted by the yellow box, and three regions of large-area non-uniformity highlighted by the green boxes. Comparing Fig. 4.6(c) with 4.6(d), and Fig. 4.6(e) with 4.6(f),we can see the clipping can remove most of the noise and mottle in the background. Furthermore, Figs. 4.6(e) and 4.6(f) show that the SSIM index image $I[m, n]$ works well for local defects, such as spots. And Figs. 4.6(c) and 4.6(d) show that the error map $E[m, n]$ can expose the defects that cover larger regions, such as large-area non-uniformities and impulse bands. By combining Fig. 4.6(d) with 4.6(f), we get the defect map $D[m, n]$ shown in Fig. 4.6(b). The two spots are enhanced by the SSIM index image $I[m, n]$. Comparing Fig. 4.6(a) with Fig. 4.6(b), we can observe that the detection map can locate both the dark and light spots, the dark impulse band along the vertical direction, the large-area non-uniformity along the image top and bottom edges, and identify a reasonable amount of graininess and streaking in the background.

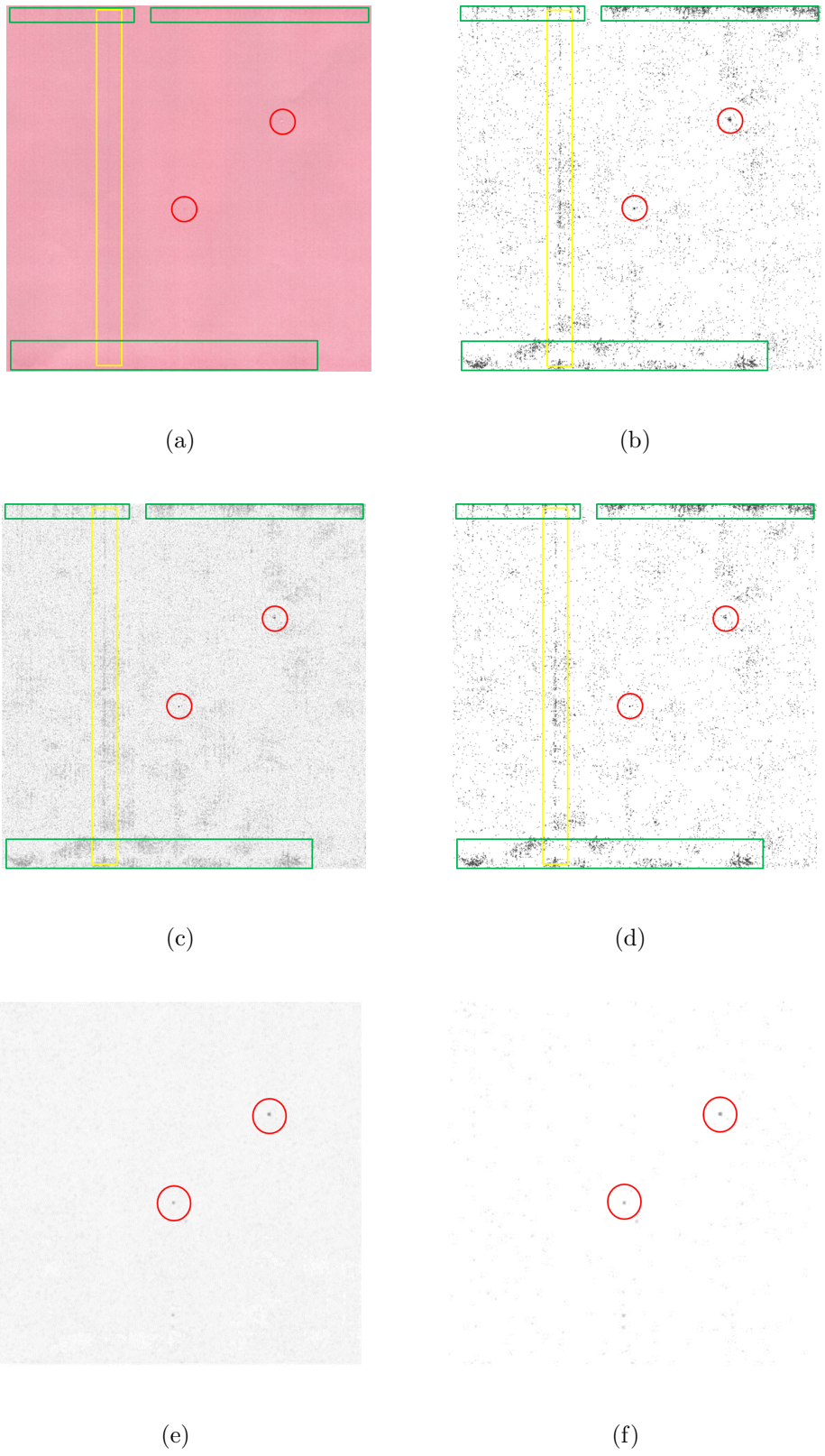

(a) (b) (c) (d) (e) (f)

Fig. 4.6. Experimental results for a ROI with multiple defects. (a) Original scanned image with defects; (b) detection map; (c) error map before clipping; (d) error map after clipping; (e) SSIM index image before clipping; (f) SSIM index image after clipping.

Figure 4.7 shows the spatial visualization results for a print document with a light impulse streak, which is highlighted with a green box. From Fig. 4.7(c) - Fig. 4.7(f), we can draw the same conclusion. The clipping can clean up most of the noise and mottle in the background, and the SSIM index image $I[m, n]$ can enhance the local defects in the defect map $D[m, n]$. Comparing the original scanned image Fig. 4.7(a) with the detection map Fig. 4.7(b), we can observe that the algorithm locates the light streak accurately with a reasonable amount of graininess in the background.

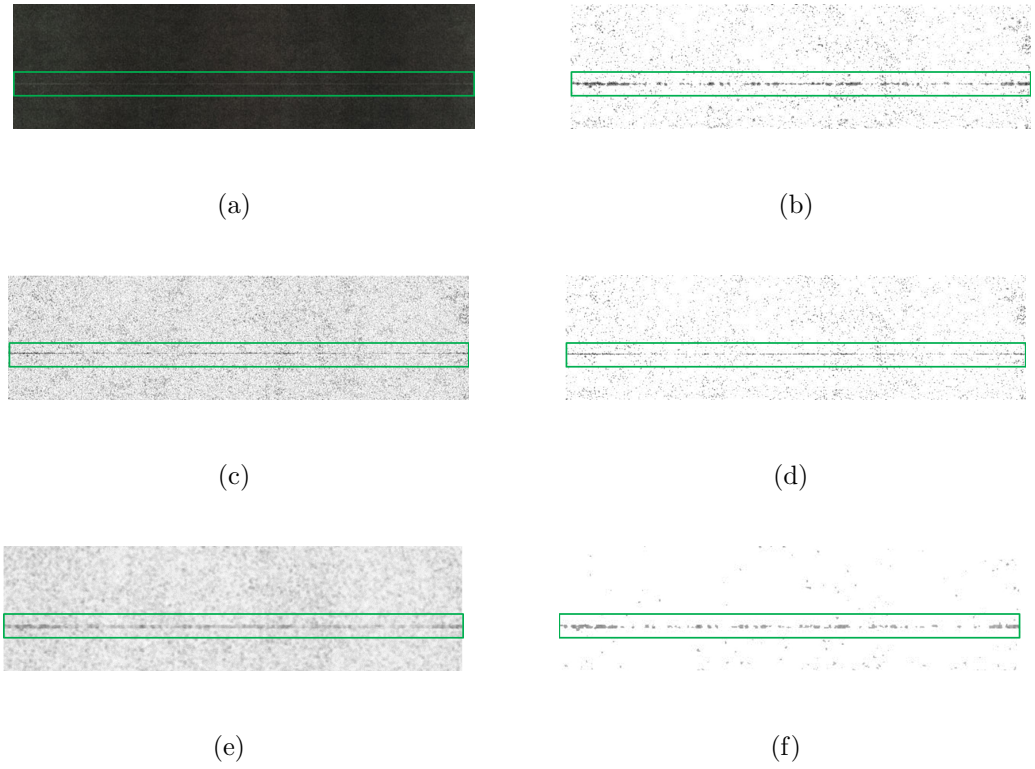


Fig. 4.7. Experimental results for a ROI with light streak. (a) Original scanned image with defects; (b) detection map; (c) error map before clipping; (d) error map after clipping; (e) SSIM index image before clipping; (f) SSIM index image after clipping.

## 4.4 Conclusion

In this chapter, we develop an image processing and analysis pipeline based on a general approach that can effectively assess the presence of a wide range of defects. The algorithm takes a digital reference or master page and the printed and scanned version of the reference page as input, then it generates a gray scale spatial visualization map that indicates the location and severity of defects as output. The defect map is based on combining an SSIM index image and an error map, which are generated by fundamentally different means. We observe that the SSIM index image $I[m, n]$ measurement works well for localized defects, such as spots; and the error map $E[m, n]$ procedure is advantageous for detecting defects that are not highly localized, such as large area nonuniformities and impulse bands. Clipping of these two components suppresses the noise in the background, while still leaving a reasonable amount of graininess, and better exposing the significant defects in the detection map $D[m, n]$. Our experimental results show promise for this general approach to detecting multiple print defects.

# 5. GHOSTING EVALUATION

## 5.1 Introduction

Ghosting is a Print Quality (PQ) defect which may appear as a single or repetitive artifact presenting vestigial objects at a certain interval as shown in Fig. 5.1. The frequency depends on the causal mechanism and the circumference of the offending rotating component. The cause of the ghosting also determines whether the ghosting is a positive(dark) or a negative(light) one. Although there are many sources of the ghosting, the most common cause is residual toner particles remain on the Organic Photo-Conductor (OPC) drum or the fuser [75–77]. If a cleaning blade does not work properly, toner particles from previous printed object near the leading edge of the page that do not fully transfer to the media/transfer belt, will transfer to the media/transfer belt during a following revolution of the OPC drum. This is the common cause of a ghosting to appear on the page along the process direction. The distance between the original object and its ghosting provides information about the circumference of the defective rotating component. The characteristic of ghosting has been well studied in reference [54]. A commercially available image analysis system to detect and quantify ghosting using Fourier analysis was developed in reference [77]. A technique that combined the human perception factor and the Fourier analysis metric to provide a final ghosting index that reflects the ghosting severity was introduced in reference [75]. A spatial analysis based on wavelet filtering and template matching in lightness channel was well defined in reference [76]. Ghosting test patterns were also designed in these existing works [53, 75–77]. However, it will be more accurate to take advantage of both the spatial analysis and Fourier analysis, finally provide one metric which also take the human perceptual factor into account.

In this chapter, we propose an algorithm for detecting and evaluating ghosting by first applying template matching in $CIE\ L^*a^*b^*$ color space, and then calculating the color difference. The template matching step in $L^*$ channel will indicate the position and the type (light or dark) of the ghosting. We then calculate the color difference among $L^*$, $a^*$, and $b^*$ to get the Delta E for evaluating purpose. We also calculate the sharpness of ghosting according to the method described in reference [75]. We will perform psychophysical experiment to study the perceptual contrast of ghosting, and then combine the sharpness metric with Delta E to improve our final evaluation in the future.

This chapter is organized as follows. Section 5.2 describes the test pattern design and the proposed algorithm for detecting and evaluating ghosting. Section 5.3 provides experimental result. We then conclude in Section 5.4.

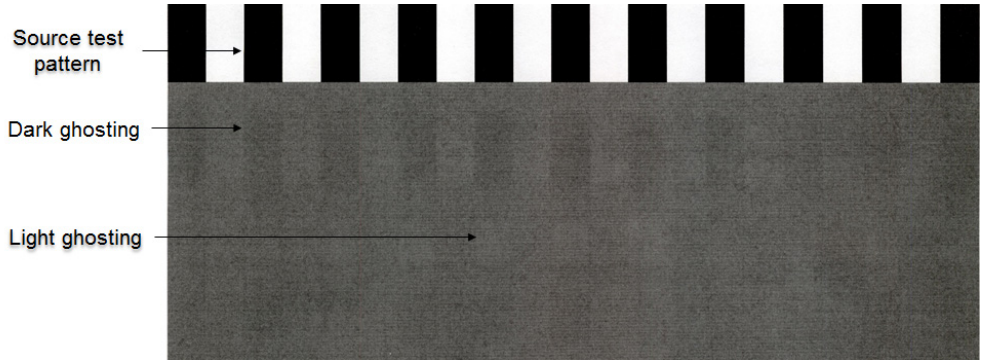


Fig. 5.1. An example of test page with source test pattern and ghosting.

## 5.2 Measurement Methodology

### 5.2.1 Test pattern design

A well-designed test page is very important for the measurement of ghosting. The test page should elicited the worst case ghosting for a printing system and the test pattern should be suitable for future analysis. Reference [75] proposes such a test

page, in which the source pattern consists of a series of black rectangular bars, and followed by a medium gray field. We use the same concept in our test pattern design.

The source test pattern, as shown in the top of Fig. 5.1, consists of 11 rectangular bars. The width of the margin between each bar is the same as the width of the black bar itself. In this way, we can have an enhanced magnitude of the ghosting in frequency domain when we do the Fourier analysis later. The height of the rectangular bars is selected according to prior knowledge of the circumferences of the rotating components. So that this test page can do the best to eliminate the possibility of overlapping between the ghosting caused by different rotating components. The test page is halftone and printed at 600 dpi, then the printout is scanned at 600 dpi.

### 5.2.2 Template matching

The bottom half part of Fig. 5.2 shows the process of the template matching algorithm. After we get the printout test pages, we first locate the Region of Interest (ROI), which is the flat medium gray field called ghosting image $G_{rgb}$. We then convert the $G_{rgb}$ from $sRGB$ to $CIE\ L^*a^*b^*$ color space and get the ghosting images of $G_l$, $G_a$, and $G_b$ in separate $L^*$, $a^*$, and $b^*$ channels. We apply template matching on $G_l$, $G_a$, and $G_b$ separately to get the 1-D profile $P_l$, $P_a$, and $P_b$ from each of them. Finally, we calculate Delta E based on the three 1-D profiles.

The major part of this algorithm is the template matching. For each ghosting image $G_l$, $G_a$, and $G_b$, we use the same method to process the image. There are two template as shown in Fig. 5.3. The left template $T_g$ in Fig. 5.3(a) starts with a white bar, and looks like an inverse version of the source test pattern. The pixel value of white region is one, and the pixel value of black region is zero. By multiplying template $T_g$ with the ROI and moving along the process direction, we are extracting the data from the potential region that ghosting might appear. To the contrary, the right template $T_b$ in Fig. 5.3(b) starts with a black bar. By multiplying template $T_b$ with the ROI and moving along the process direction, we will extract the average value

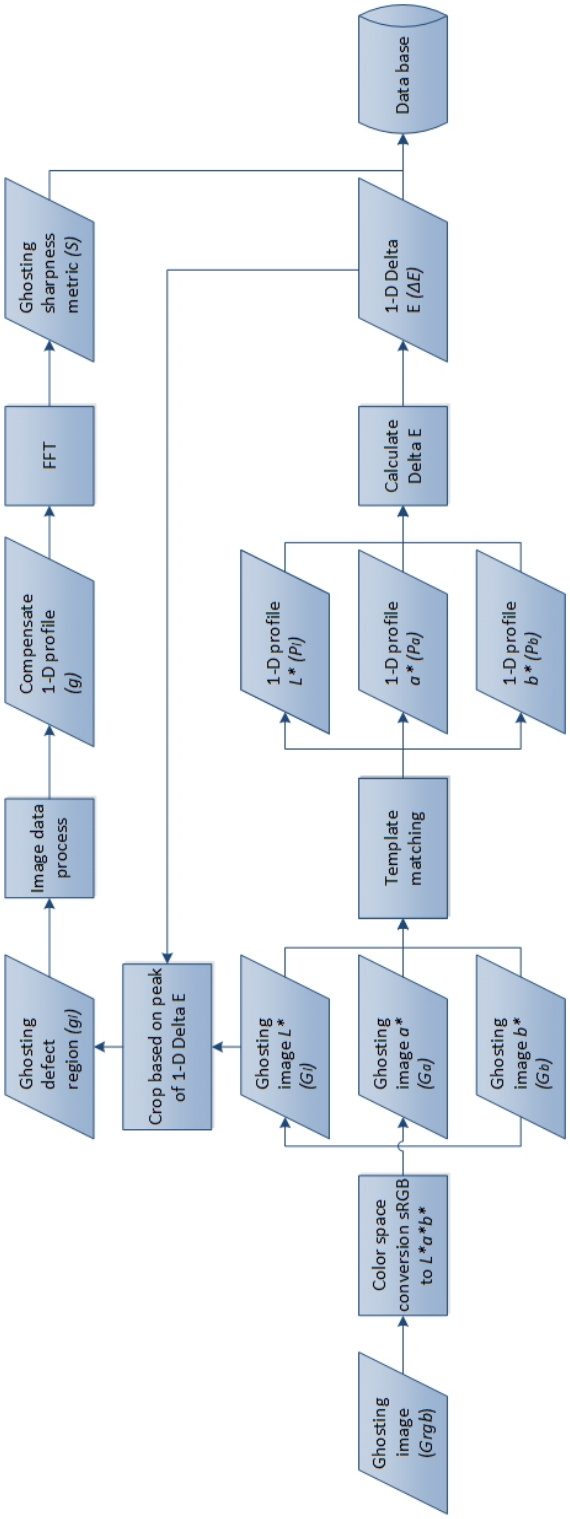


Fig. 5.2. Overview of the ghosting detection and evaluation algorithm.

from the background. Therefore, we define the 1-D profile $P_j$ from $G_j$ $(j = l, a, b.)$ and $T_k$ $(k = g, b.)$ as

$$P_{jk}(i) = \frac{\sum_{m=i}^{m=i+h+1} \sum_{n=1}^{n=W} G_j[m,n] \cdot T_k[m-i+1,n]}{\sum_{m=i}^{m=i+h+1} \sum_{n=1}^{n=W} T_k[m-i+1,n]}, \tag{5.1}$$

and

$$p_j(i) = P_{jg}(i) - P_{jb}(i). \tag{5.2}$$

Where $i = 1, \cdots, H-h+1$; $j = l, a, b$; $k = g, b$. H is the height of the ROI, which in this case is the height of $G_l$, $G_a$, and $G_b$; W is the width of the ROI; h is the height of the source test pattern. By taking difference between $P_{jg}$ and $P_{jb}$, we are actually subtracting the background value that surround the ghosting and get the magnitude of the difference between the ghosting and non-ghosting regions. In this way, we can eliminate the effect of the noise and the low fluctuation in the background. The sign of $P_l$ will indicate the type (light or dark) of the ghosting.

After getting the 1-D profile of each color channel, we then define the 1-D Delta E as

$$\Delta E(i) = \sqrt{\left(P_l(i) - \overline{P_l}\right)^2 + \left(P_a(i) - \overline{P_a}\right)^2 + \left(P_b(i) - \overline{P_b}\right)^2}, \tag{5.3}$$

where $\overline{P_l}$, $\overline{P_a}$, and $\overline{P_b}$ are the mean value of $P_l$, $P_a$, and $P_b$, respectively. The peak(s) in 1-D Delta E indicate(s) the start position of the ghosting, the sign of that point in $P_l$ indicates the type of the ghosting. For the record, we focus on achromatic test pages for now. As we know, human eye is more sensitive to changes in gray levels, and a difference of 0.5 Delta E might be noticeable to experts. Therefore, we then define one Delta E as the threshold of pass or fail. If the value of the peak in 1-D Delta E is less than 0.5, then the relative ghosting has a rank A; if it is between 0.5 to 1, then the relative ghosting has a rank B; between 1 to 1.5, then the relative ghosting has a rank C; if it is larger than 1.5, then the relative ghosting has a rank D. Test pages with rank A and B are acceptable and those with rank C and D are unacceptable.

(a) (b)

Fig. 5.3. Templates used in the template matching. (a) Template for potential ghosting region $T_g$; (b) template for background region $T_b$.

### 5.2.3 Sharpness calculation

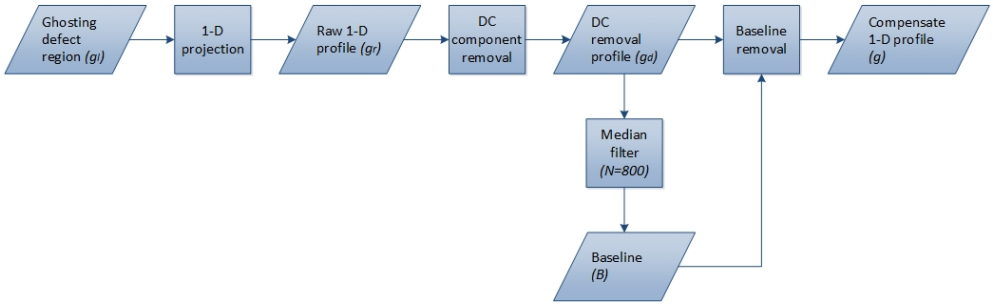


Fig. 5.4. Process of getting compensate 1-D profile.

After we get the position of the interested ghosting, we then crop the defect region $g_l$ in $L^*$ channel and do Fourier analysis to get the sharpness metric of it, which is shown in the top half of Fig. 5.2. To prepare the data before performing FFT, we perform the following steps as shown in Fig. 5.4 to get the compensate 1-D profile $g$. First, we do a 1-D projection on the ghosting defect region $g_l$ to get the raw 1-D profile $g_r$. We then remove the DC component, and further apply a median filter with window size 800 on the DC removal profile $g_d$ to get a baseline $B$. After subtracting the baseline $B$ from DC removal profile $g_d$, we achieve the compensate 1-D profile $g$. Example of the four 1-D profiles are shown in Fig. 5.5.

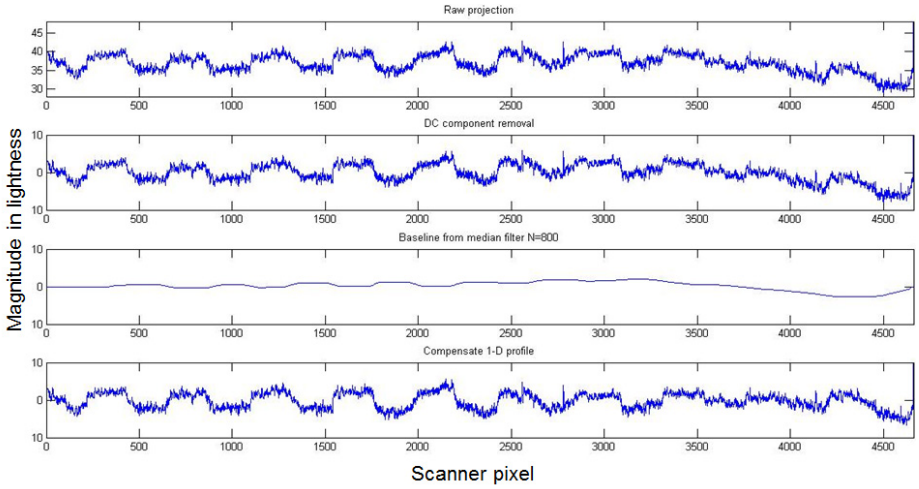


Fig. 5.5. Example of the four 1-D profiles.

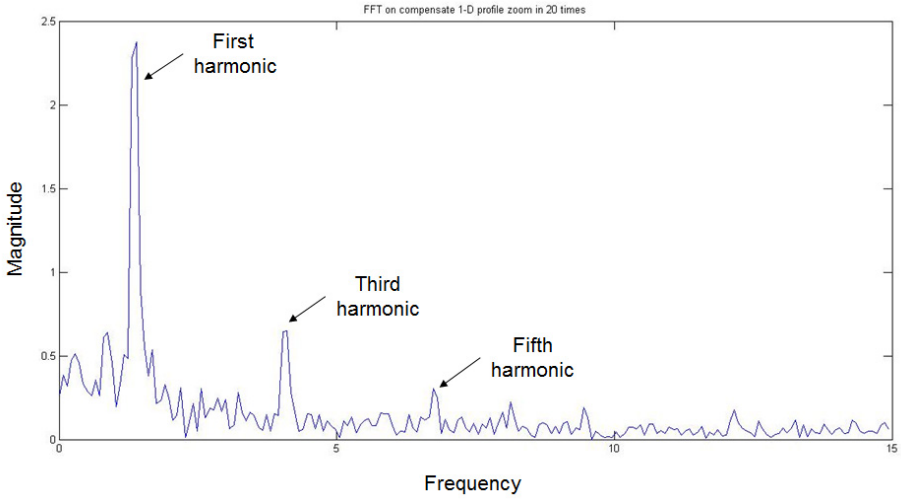


Fig. 5.6. Example of the compensate 1-D profile in frequency domain.

Figure 5.6 is an example of the compensate 1-D profile $g$ in frequency domain. We then define the sharpness of the ghosting edges according to reference [75] as

$$sharpness = \frac{First}{Third \cdot Fifth^2}, \tag{5.4}$$

where $First$, $Third$, and $Fifth$ indicate the magnitude of First harmonic, Third harmonic, and Fifth harmonic as shown in Fig. 5.6. This metric represent an overall ghosting sharpness of the vertical edges in the ghosting defect region.

## 5.3 Experimental Result

In this section, we show the experimental result. The algorithm of template matching and Delta E calculation is applied on a real sample with both dark ghosting and light ghosting. Figure 5.7 is presenting the final Delta E on the top of that real sample. On the top left of the evaluated result image, there are ranks and types of the ghosting defect that present in this target sample. If it is a dark ghosting the peak of the Delta E would point to left from the center black line of the image, and if it is a light ghosting the peak of the Delta E would point right from the center black line of the image. We locate the ghosting peaks by highlighting them, and pointing to the rulers along both the left and right sides. The number shows on the ruler indicates the circumference of the defective rotating component. The slope of the Delta E around the peak which highlight the ghosting indicate the sharpness of the ghosting along the top and bottom edges. While the sharpness metric that we calculate by using Fourier analysis is indicating an overall sharpness of the ghosting along the vertical edges of each bar.

We further test the algorithm on 82 samples. The evaluation time taken by the expert was about two and half hours. While our algorithm evaluated the samples four second per page. Figure 5.8 shows the comparison of the evaluation result between our algorithm and the expert visual score, the matching accuracy for pass or fail is 92%.

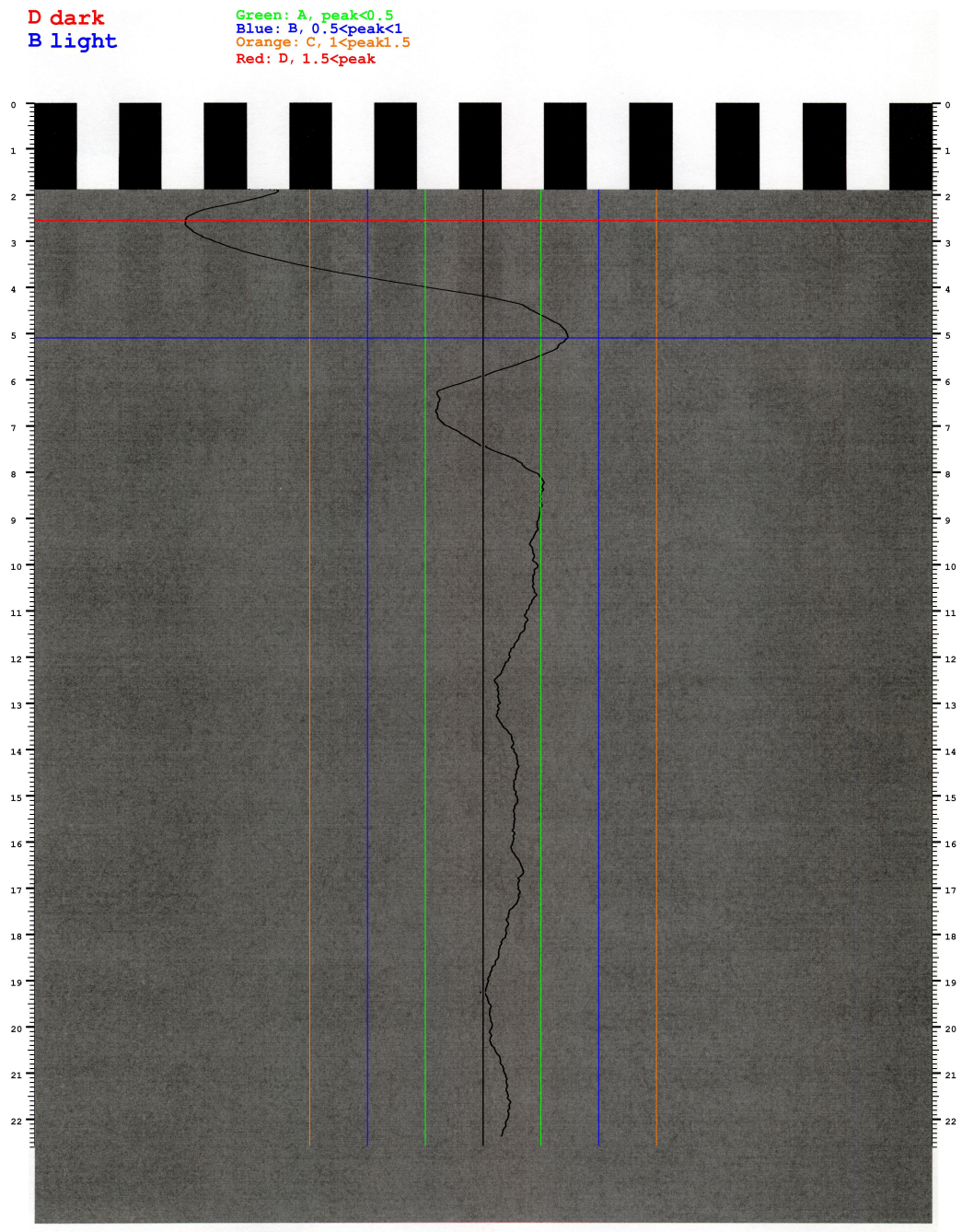


Fig. 5.7. Example evaluation result on a real printout document sample.

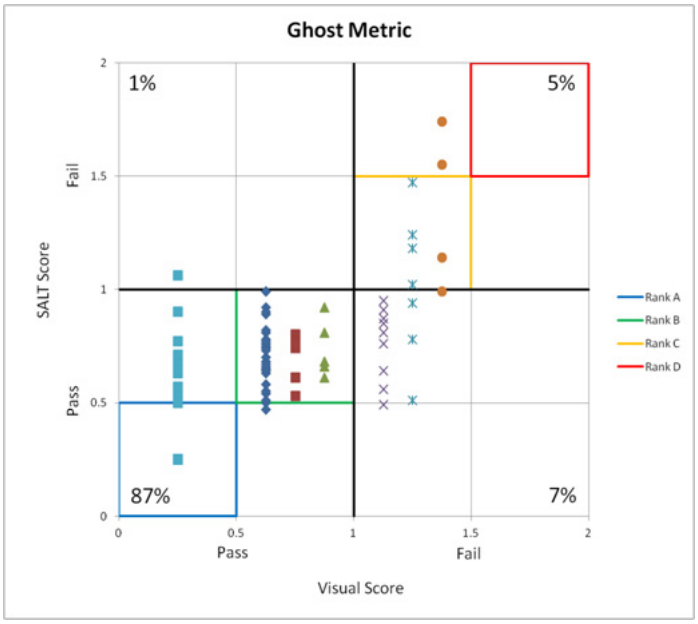


Fig. 5.8. Comparison of the evaluation result between our algorithm and the expert visual score.

## 5.4 Conclusion

This chapter presents an algorithm for detecting and evaluating the ghosting defects in EP printers, including a test pattern design. Template matching and Delta E calculation extract the ghosting position and evaluate the ghosting severity. The sharpness metric can provide the edge information of the ghosting defect region. Our experimental results show promise for this whole process to detect and evaluate ghosting with high accurate rate and efficiency compare with human visual evaluation.

# LIST OF REFERENCES

# LIST OF REFERENCES


[1] D. Silverstein and J. Farrell, "The relationship between image fidelity and image quality," *Proc. of the IEEE*, vol. 1, pp. 881–884, 1996.

[2] J. Lubin, "A visual discrimination model for imaging systems design and evaluation," in *Vision Models for Target Detection and Recognition* (E. Peli, ed.), pp. 245 – 283, Singapore: World Scientific, 1995.

[3] X. Zhang and B. A. Wandell, "Color image fidelity metrics evaluated using image distortion maps," *Signal Processing*, vol. 70, no. 3, pp. 201–214, 1998.

[4] M. Eskicioglu and P. Fisher, "Image quality measures and their performance," *IEEE Trans. on Communications*, vol. 43, no. 12, pp. 2959–2965, 1995.

[5] A. Watson, "The cortex transform rapid computation of simulated neural images," *Comput. Vision Graphics and Image Process.*, vol. 39, no. 3, pp. 311–327, 1987.

[6] S. Daly, "The visible differences predictor: An algorithm for the assessment of image fidelity," in *Digital Images and Human Vision* (A. B. Watson, ed.), pp. 179–205, Cambridge, MA: MIT Press, 1993.

[7] P. C. Teo and D. J. Heeger, "Perceptual image distortion," *Proc. SPIE*, vol. 2179, pp. 127–141, 1994.

[8] D. J. Heeger and P. C. Teo, "A model of perceptual image fidelity," in *Proc. of IEEE Int'l Conf. on Image Proc.*, (Washington, D.C., USA), pp. 343 – 345, Oct. 23 – 26 1995.

[9] S. J. P. Westen, R. L. Lagendijk, and J. Biemond, "Perceptual image quality based on a multiple channel HVS model," in *Proc. of IEEE Int'l Conf. on Acoust., Speech and Sig. Proc.*, pp. 2351 – 2354, 1995.

[10] C. C. Taylor, Z. Pizlo, J. P. Allebach, and C. A. Bouman, "Image quality assessment with a Gabor pyramid model of the human visual system," in *Human Vision and Electronic Imaging*, vol. SPIE 3016, (San Jose, CA, USA), pp. 58 – 69, Feb. 8 – 14 1997.

[11] C. C. Taylor, J. P. Allebach, and Z. Pizlo, "The image fidelity assessor," *Proc. of the IS&T Image Processing, Image, Quality, and Image Capture Systems Conference*, pp. 237–241, 1998.

[12] V. R. Avadhanam, N. and V. R. Algazi, "Evaluation of a human vision system based image fidelity metric for image compression," *Applications of Digital Image Processing XXII*, pp. 569–579, 1999.

[13] R. Mantiuk, K. Myszkowski, and H. P. Seidel, "Visible difference predictor for high dynamic range images," *Proc. of IEEE International Conference on System, Man and Cybernetics*, pp. 2763–2769, 2004.

[14] W. Wu, "Two problems in digital color imaging: colorimetry and image fidelity assessor," *Ph. D. dissertation*, 2000.

[15] T. J. Doll, S. W. McWhorter, W. A. A., and D. E. Schmieder, "Robust, sensor-independent target detection and recognition based on computational models of human vision," *Optical Engineering*, vol. 37, pp. 2006–2021, 1998.

[16] E. W. Jin, X. Feng, and J. Newell, "The development of a color visual difference model (cvdm)," *Proc. of the IS&T Image Processing, Image, Quality, and Image Capture Systems Conference*, pp. 154–158, 1998.

[17] E. W. Jin, X. Feng, and J. Newell, "Image evaluation using a color visual difference predictor (cvdp)," *Human Vision and Electronic Imaging*, pp. 175–186, 2001.

[18] G. Ramanarayanan, B. Ferwerda, J.and Walter, and K. Bala, "Visual equivalence: Towards a new standard for image fidelity," *ACM Transactions on Graphics (TOG)*, vol. 26, no. 3, pp. 76–87, 2007.

[19] X. Jing, H. Nachlieli, D. Shaked, S. Shiffman, and J. P. Allebach, "Masking mediated print defect visibility predictor," *Proc. SPIE*, vol. 8293, p. 82930R, 2012.

[20] Z. Wang, A. C. Bovik, H. R. Sheikh, and E. P. Simoncelli, "Visual equivalence: Towards a new standard for image fidelity," *IEEE Trans. on Image Processing*, vol. 13, no. 4, pp. 600–612, 2004.

[21] C. Li and A. C. Bovik, "Content-partitioned structural similarity index for image quality assessment," *Signal Processing*, vol. 25, no. 7, pp. 517–526, 2010.

[22] S. S. Channappayya, A. C. Bovik, and R. Heath, "Rate bounds on ssim index of quantized image dct coefficients," *IEEE Trans. on Image Processing*, vol. 17, no. 9, pp. 1057–7149, 2008.

[23] B. Min, Z. Pizlo, and J. P. Allebach, "Development of softcopy environment for primary color banding visibility assessment," *Proc. SPIE*, vol. 68080A, p. 12, 2008.

[24] O. Arslan, Z. Pizlo, and J. P. Allebach, "Softcopy banding visibility assessment," *Journal of Imaging Science and Technology*, vol. 51, no. 3, pp. 271–281, 2007.

[25] Y. Bang, Z. Pizlo, N. Burningham, and J. P. Allebach, "Discrimination based banding assessment," *Proc. IS&Ts NIP19*, pp. 745–750, 2003.

[26] Y. Bang, Z. Pizlo, and J. P. Allebach, "Banding assessment with controlled halftoning: The ten printer experiment," *Journal of Imaging Science and Technology*, vol. 50, pp. 522–529, 2006.

[27] T. Ha, J. P. Allebach, and D. Cha, "Measurement and analysis of banding artifacts in color electrophotographic printers," *Proc. IS&Ts NIP24*, pp. 7–12, 2008.

[28] H. Nachlieli, "Automatic mechanical-band perceptual evaluation," *Proc. IS&Ts NIP25*, pp. 495–498, 2009.

[29] H. Nachlieli and D. Shaked, "Measuring the quality of quality measures," *IEEE Trans. on Image Processing*, vol. 20, pp. 76–87, 2011.

[30] N. A. Rawashdeh, I. Shin, K. Donohue, and S. Love, "Printer banding estimation using the generalized spectrum," *Proc. of SPIE-IS&T*, pp. 6059–15, 2006.

[31] C. Cui, D. Cao, and S. T. Love, "Measuring visual threshold of inkjet banding," *Proc. of IS&T's PICS*, pp. 84–89, 2001.

[32] Z. Fan, W. Wu, E. Dalal, and R. Rasmussen, "Robust estimation of print mottle," *Proc. SPIE 6808*, vol. 680808, pp. 1–7, 2008.

[33] A. Eid, B. E. Copper, and E. E. Rippetoe, "Characterization of mottle and low-frequency print defects," *Proc. SPIE 6808*, vol. 680808, p. 12, 2008.

[34] E. Bernal, J. P. Allebach, and J. Trask, "Model-based memory-efficient algorithm for compensation of toner overdevelopment in electro-photographic printers," *Journal of Imaging Science and Technology*, vol. 52, no. 6, pp. 060504–1–15, 2008.

[35] P. H. J. and J. P. Allebach, "A psychophysical investigation of the effect of coring on perceived toner scatter," *Journal of Electronic Imaging*, vol. 19, no. 1, p. 011008, 2010.

[36] K. D. Donohue, M. V. Venkatesh, and C. Cui, "Prediction of print defect perception," *Proc. of IS&T's PICS*, pp. 44–49, 2003.

[37] K. D. Donohue, C. Cui, and M. V. Venkatesh, "Wavelet analysis of print defects," *Proc. of IS&T's PICS*, pp. 42–47, 2002.

[38] A. Eid, B. Cooper, and E. Rippetoe, "A unified framework for physical print quality," *Proc. of SPIE 6494*, pp. 64940C–11, 2007.

[39] P. J. Kane, T. F. Bouk, P. D. Burns, and A. D. Thompson, "Quantification of banding, streaking and grain in flat field images," *Proc. of IS&T's PICS*, pp. 79–83, 2000.

[40] G. E. Legge and J. M. Foley, "Contrast masking in human vision," *Journal of the Optical Society of America*, vol. 70, no. 12, pp. 1458–1471, 1980.

[41] W. A. B. and J. A. Solomon, "Model of visual contrast gain control and pattern masking," *Journal of the Optical Society of America*, vol. A, no. 14, pp. 2379–2391, 1997.

[42] A. Saadane, "Watermark strength determination based on a new contrast masking model," *Proc. of SPIE 5020*, vol. 5020, pp. 107–114, 2003.

[43] P. G. J. Barten, "Simple model for spatial-frequency masking and contrast discrimination," *Proc. of SPIE 2411*, p. 142, 1995.

[44] L. Barghout-Stein, C. W. Tyler, and S. A. Klein, "Partitioning mechanisms of masking: contrast transducer versus divisive inhibition," *Proc. of SPIE 3016*, p. 25, 1997.

[45] A. B. Watson, "Image quality and entropy masking," *Proc. of SPIE 3016*, pp. 2–12, 1997.

[46] D. M. Chandler, K. H. S. Lim, and S. S. Hemami, "Effects of spatial correlations and global precedence on the visual fidelity of distorted images," *Proc. of SPIE 6057*, pp. 60570F–15, 2006.

[47] B. W. Keelan, *Handbook of Image Quality: Characterization and Prediction*. CRC Press, 2002.

[48] D. R. Rasmussen, K. D. Donohue, Y. S. Ng, W. C. Kress, F. Gaykema, and S. Zoltner, "ISO 19751 macro-uniformity," *Image Quality and System Performance, Proc. SPIE*, vol. 6059, 2006.

[49] D. R. Rasmussen, K. D. Donohue, Y. S. Ng, W. C. Kress, F. Gaykema, and S. Zoltner, "W1.1 macro-uniformity," *Image Quality and System Performance, Proc. SPIE*, vol. 7242, 2009.

[50] I. 20462-3, "photography - psychophysical experimental methods to estimate image quality - part 3: Quality ruler method,"

[51] P. D. Burns, J. B. Phillips, and D. Williams, "Adapting iso 20462 softcopy quality ruler method for on-line image quality studies," *Image Quality and System Performance X, Proc. SPIE*, vol. 8653, 2013.

[52] W. Wang, G. Overall, T. Riggsb, R. Silveston-Keithb, J. Whitneyb, G. Chiuc, and J. P. Allebacha, "Figure of merit for macro-uniformity based on image quality ruler evaluation and machine learning framework," *Image Quality and System Performance X, Proc. SPIE*, vol. 8653, 2013.

[53] W. Y. Jang, M. Chen, J. P. Allebach, and G. T. Chiu, "Print quality test page," *Journal of Imaging Science and Technology*, vol. 48, no. 5, pp. 432–446, 2005.

[54] W. Y. Jang and J. P. Allebach, "Simulation of print quality defects," *Journal of Imaging Science and Technology*, vol. 49, no. 1, pp. 1–18, 2005.

[55] S. Hu, J. P. Allebach, H. Nachieli, D. Shaked, and S. Shiffman, "Color-dependent banding characterization and simulation on natural document images," *Proc. of SPIE*, vol. 8292, p. 34, 2012.

[56] P. E. King-Smith and J. J. Kulikowski, "Pattern and flicker detection analyzed by subthreshold summation," *Journal of Physiology (London)*, vol. 249, no. 3, pp. 56P–57P, 1975.

[57] C. C. Taylor, "Image quality assessment based on a human visual system model," 1998.

[58] J. M. Foleya and G. E. Leggea, "Contrast detection and near-threshold discrimination in human vision," *Vision research*, vol. 21, pp. 1041–1053, 1981.

[59] D. J. Finnney, *Probit analysis*. Cambridge Univ. Press, 1971.

[60] J. Zhang, J. P. Allebach, H. Nachieli, D. Shaked, and S. Shiffman, "Psychophysical evaluation of banding visibility in the presence of print content," *Proc. of SPIE*, vol. 8293, p. 27, 2012.

[61] S. Kim and J. P. Allebach, "Optimal unsharp mask for image sharpening and noise removal," *Journal of Electronic Imaging*, vol. 14, no. 2, p. 023005, 2005.

[62] B. Zhang and J. P. Allebach, "Adaptive bilateral filter for sharpness enhancement and noise removal," *IEEE Trans. on Image Processing*, vol. 17, no. 5, pp. 664–678, 2008.

[63] R. Bergman, H. Nachlieli, and G. Ruckenstein, "Detection of textured areas in natural images using an indicator based on component counts," *Journal of Electronic Imaging*, vol. 17, no. 4, p. 043003, 2008.

[64] E. J. Delp and O. R. Mitchell, "Image coding using block truncation coding," *IEEE Trans. on Communications*, vol. 27, pp. 1335–1342, 1979.

[65] E. Hasanbelliu and J. a. P. J. Kampa, K. abd Cobb, "Image coding using block truncation coding," *Proc. of SPIE*, vol. 8017, p. 80170S, 2011.

[66] R. Achanta, S. Hemami, F. Estrada, and S. Susstrunk, "Frequency-tuned salient region detection," *CVPR*, p. 12, 2009.

[67] H. Nachlieli, Z. Karni, and S. Raz, "Perception guided automatic press diagnosis," *Proc. IS&Ts NIP27*, pp. 784–787, 2011.

[68] A. Eid, M. Ahmed, B. Cooper, and E. Rippetoe, "Characterization of electrophotographic print artifacts:banding, jitter, and ghosting," *IEEE Trans. on Image Processing*, vol. 20, no. 5, pp. 1313–1326, 2011.

[69] D. R. Rasmussen, F. Gaykema, Y. S. Ng, K. D. Donohue, W. C. Kress, and S. Zoltner, "W1.1 macro-uniformity," *Image Quality and System PerformanceVI, Proc. of SPIE*, vol. 7242, pp. S. P. Farnand and F. Gaykema, eds. 724204–1, 2009.

[70] D. R. Rasmussen, "Tent-pole spatial defect pooling for prediction of subjective quality assessment of streaks and bands in color printing," *Journal of Electronic Imaging*, vol. 19, no. 1, p. 011017, 2010.

[71] Q. Guo and Z. Wei, "Tire defect detection using image component decomposition," *Journal of Applied Sciences, Engineering and Technology*, vol. 4, no. 1, pp. 41–44, 2012.

[72] E. K. Zeise, D. R. Rasmussen, Y. S. Ng, E. Dalal, A. McCarthy, and D. Williams, "Incits w1.1 development update: Appearance-based image quality standards for printers," *Image Quality and System Performance V, Proc. of SPIE*, vol. 6808, pp. S. P. Farnand and F. Gaykema, eds. 680802–1, 2008.

[73] K.-Y. Lee, Y. Bang, and H.-K. Choh, "Quantification of perceived macro-uniformity," *Image Quality and System Performance VIII, Proc. of SPIE*, vol. 7867, pp. S. P. Farnand and F. Gaykema, eds. 786704–1, 2011.

[74] O. Barkol, H. Kogan, D. Shaked, and M. Fischer, "A robust similarity measure for automatic inspection," *Proc. of IEEE Int'l Conf. on Image Proc.*, pp. 2489–2492, 2010.

[75] P. L. Jeran and N. Burningham, "Measurement of electrophotographic ghosting," *Proc. of IS&T's PICS*, pp. 80–83, 2001.

[76] A. H. Eid, B. E. Cooper, and M. N. Ahmed, "Characterization of ghosting defects in electrophotographic printers," *Proc. of IEEE Int'l Conf. on Image Proc.*, vol. 3, pp. 453–456, 2007.

[77] J. Briggs, E. Hong, and D. Forrest, "Analysis of ghosting in electrophotography," *Proc. IS&Ts NIP16*, pp. 403–407, 2000.

VITA

# VITA

Xiaochen Jing received her BS degree in Electrical Engineering from Tongji University, Shanghai, China, in 2007. Since 2008, she has been working towards her Ph.D. degree in Purdue University, West Lafayette, IN. She received her MSEE and Ph.D. degree in Electrical and Computer Engineering from Purdue University, West Lafayette, IN in 2011 and 2013, respectively. Her research interests include image processing, image quality, computer vision, print quality, psychophysics, and human perception.